Supplementary Information for
Mutually-Dependent Kinetics and Energetics of Photocatalyst/Co-Catalyst/ Two-Redox Liquid Junctions

Zhenhua Pan[ab †], Rito Yanagi[ab †], Qian Wang[c], Xin Shen[ab], Qianhong Zhu[ab], Yudong Xue[abd], Jason A. Röhr [ab], Takashi Hisatomi[e], Kazunari Domen[ef], Shu Hu[*ab]

[a] Department of Chemical and Environmental Engineering, Yale University, New Haven, CT 06520 (USA)

[b] Energy Sciences Institute, Yale University, 810 West Campus Drive, West Haven, CT 06516 (USA)

[c] Department of Chemical System Engineering, School of Engineering, The University of Tokyo, 7-3-1 Hongo, Bunkyo-ku, Tokyo 113-8656 (Japan)

[d] National Engineering Laboratory for Hydrometallurgical Cleaner Production Technology, CAS Key Laboratory of Green Process and Engineering, Institute of Process Engineering, Chinese Academy of Sciences, Beijing 100190 (China)

[e] Research Initiative for Supra-Materials, Shinshu University, 4-17-1 Wakasato, Nagano-shi, Nagano 380-8553, (Japan)

[f] Office of University Professor, The University of Tokyo, 7-3-1 Hongo, Bunkyo-ku, Tokyo 113-8656 (Japan)

[†] Both authors contributed equally to this manuscript.

Contents

Materials and Methods

1. Single-crystalline $SrTiO_3$ photoelectrode preparation. Single crystals of (100)-oriented $SrTiO_3$ were obtained from MTI corporation. To achieve n-type doping, the sample was heated at 1000 °C for 4 h under a flow of H_2 gas and was subsequently allowed to cool down naturally.[1] The colour of the resulting crystal was lightly black due to the introduction of oxygen vacancies and/or titanium interstitials. The free-electron concentration was estimated to be 1×10^{18} cm^{-3}.[2] A Ga:In eutectic mixture was pasted on the back of the sample. A Sn wire was then connected to the back with Ag glue and the electrode was insulated with epoxy. Prior to all experiments, the electrode was etched in 10 vol% HNO_3 (aq) for 1 min, followed by rinsing with deionized water.

2. Al-doped $SrTiO_3$ particles, particle-based Al-doped $SrTiO_3$ and Al-doped $SrTiO_3/RhCrO_x$ photoelectrode preparation. Al-doped $SrTiO_3$ particles (denoted as $SrTiO_3$:Al) were prepared using a flux method.[3] $SrTiO_3$ (Wako Pure Chemicals Industries, Ltd., 99.9%), Al_2O_3 (Sigma-Aldrich Co., LLC., nanoparticle), and $SrCl_2$ (Kanto Chemicals Co., Inc., 98.0%, anhydrous) were mixed at a molar ratio of 1:0.02:10 and the mixture was heated at 1100 °C for 10 h in air. The product was washed in deionized water to obtain $SrTiO_3$:Al. Successful synthesis of $SrTiO_3$:Al was confirmed by a X-ray diffraction (XRD) as shown in Figure S31a. The free-electron concentration of $SrTiO_3$:Al was less than 1.0×10^{17} cm^{-3}.[4] Particle-based $SrTiO_3$:Al electrodes (denoted as Ti/$SrTiO_3$:Al) were prepared by immobilizing $SrTiO_3$:Al particles onto a 5 μm-thick conductive Ti layer using a particle transfer method.[5] $SrTiO_3$:Al particles (0.01 g) were dispersed in isopropanol (0.5 mL) by ultrasonication. The suspension was drop-cast onto a glass substrate and was allowed to dry naturally. A 5 μm-thick Ti layer was deposited on the particles-on-glass substrate by radio-frequency magnetron sputtering. A second glass substrate with adhesive epoxy was used to lift off the Ti layer containing the particles. The immobilization of $SrTiO_3$:Al particles on a Ti layer was confirmed by scanning electron microscopy (SEM) as shown in Figure S32. A Ga:In eutectic mixture was pasted on the Ti layer. A Sn wire was connected to the region with Ga:In mixture by Ag glue and the electrode was insulated with epoxy. Excess particles loosely attached to the particle photoelectrodes were removed by ultrasonication in deionized water. $RhCrO_x$ as a co-catalyst was loaded onto the $SrTiO_3$:Al particles before assembling them to make photoelectrodes. Particle-based $SrTiO_3$:Al/$RhCrO_x$ electrodes (denoted as Ti/$SrTiO_3$:Al/$RhCrO_x$) were prepared following the same procedures as the $SrTiO_3$:Al electrodes.

3. Ta_3N_5 photoelectrodes and Ta_3N_5 particles preparation. A native TaO_x layer can form on the surface of Ta_3N_5 particles and this oxide layer would reduce the conductivity if the particles were loaded on a conductive substrate by a particle transfer method similar to that for $SrTiO_3$.[6] Therefore, Ta_3N_5 thin films were directly grown on a Ta substrate by a sequential sputtering and nitridation process.[6] An 500 nm-thick TaO_x particle film was sputtered on a Ta substrate by radio-frequency magnetron sputtering. The Ta/TaO_x film was nitridated at 800 °C for 1 h in an NH_3 flow (300 mL min^{-1}) with a temperature ramp of 10 °C min^{-1}. The resulting thin film is denoted as Ta/Ta_3N_5. Its morphology was confirmed by SEM as shown in Figure S19. A Ga:In eutectic mixture was pasted onto the back side of the Ta layer. A Sn wire was connected to the region with Ga:In mixture by Ag glue and the electrode was packaged with insulating epoxy. Ta_3N_5 particles were prepared by thermal nitridation of Ta_2O_5 (Rare Metallic Co., Ltd., 99.99%) under the same condition. The crystal structures of Ta_3N_5 thin film on Ta substrate and the Ta_3N_5 particles were confirmed by XRD as shown in Figure S31b. The resulting charge-carrier concentration was previously reported to be ca. 1.0×10^{19} cm^{-3}.[7]

4. Co-catalyst deposition on photoelectrodes. Pt was electro-deposited on single-crystalline $SrTiO_3$ electrodes (donated as $SrTiO_3$/Pt) and Ta/Ta_3N_5 electrodes (donated as Ta/Ta_3N_5/Pt) using a 10 mg·mL^{-1} H_2PtCl_6 (Aldrich, 99.9%) aqueous solution. During the deposition process, the applied potential was cycled from −0.3 to 0.1 V vs. SCE twice. To avoid the deposition of Pt on the Ti layer, Pt was photo-deposited on Ti/$SrTiO_3$:Al electrodes using the same Pt source (donated as Ti/$SrTiO_3$:Al/Pt). The electrodes were illuminated using a laser-driven Xe lamp (λ = 170 ~ 800 nm, EQ-99X LDLS, Energetiq Technology, Inc) during the 30-min deposition process. A Cr_2O_3 layer was electrodeposited on $SrTiO_3$/Pt (donated as $SrTiO_3$/(Cr_2O_3/Pt)) using a 100 mg·mL^{-1} K_2CrO_4 (Sigma-Aldrich Co., LLC., 99%) aqueous solution. During the deposition process, a potential of −1.0 V vs. SCE was applied on the electrode for 5 h. The electrolyte was bubbled with N_2 gas for 20 minutes to purge dissolved O_2 before the deposition process.

5. Co-catalyst deposition on photocatalysts. Pt (3 wt%) was loaded on $SrTiO_3$: Al particles (donated as $SrTiO_3$:Al/Pt) and Ta_3N_5 particles (donated as Ta_3N_5/Pt) by photo-deposition in a top-irradiation-type reaction cell. Photocatalysts (0.1 g) were dispersed

in 100 mL deionized water (for $SrTiO_3$:Al) or in a 20 vol% methanol aqueous solution (for Ta_3N_5) containing H_2PtCl_6 (Aldrich, 99.9%, the weight of Pt equals 3 wt% photocatalysts). Prior to performing the reaction, the cell was evacuated to remove air and dissolved O_2 in the water and was then filled with Ar. The solution was illuminated for 3 h using a 300 W Xe lamp ($\lambda > 300$ nm), equipped with an all-reflection mirror. After photo-deposition, the suspension was filtered and the obtained particles were washed with deionized water. $RhCrO_x$ (0.1 wt% Rh and 0.1 wt% Cr) was loaded onto the $SrTiO_3$:Al particles using an impregnation method. $SrTiO_3$:Al particles were dispersed in an aqueous solution containing Na_3RhCl_6 (Mitsuwa Chemistry Co., Ltd., 17.8 wt%, the weight of Rh equals 0.1 wt% $SrTiO_3$:Al particles) and $Cr(NO_3)_3$ (Kanto Chemicals Co., Inc., 98.0 – 103.0%, the weight of Cr equals 0.1 wt% $SrTiO_3$:Al particles). After the solution was evaporated in a water bath, the precipitated solids were calcined in air at 350 °C for 1 h.

6. Co-catalyst deposition on F-doped SnO_2 electrodes. Similar to the single crystal $SrTiO_3$ electrodes, Pt was electro-deposited on F-doped SnO_2 (FTO) electrodes. These electrodes are denoted as FTO/Pt. $RhCrO_x$ (0.1 wt% Rh and 0.1 wt% Cr) was loaded onto the FTO electrodes by a similar impregnation method as was used for the $SrTiO_3$:Al particles. In this case, the precursor solution was dried naturally instead of using a water bath. The resulting electrodes are denoted as FTO/$RhCrO_x$.

7. Electrochemical measurements. The electrochemical properties of the electrodes were measured at 25 °C in a three-electrode system consisting of a working electrode, an alkaline Hg/HgO reference electrode, and a carbon rod counter electrode. The electrolyte was a 0.5 M Na_2SO_4 (Sigma-Aldrich Co., LLC., 99%) aqueous solution at pH 12.5 adjusted by KOH (Sigma-Aldrich Co., LLC., 99.99%). The measured potentials were converted to reversible hydrogen electrode (RHE) scale according to the following equation:

$V_{RHE} = V_{Hg/HgO} + V^o_{Hg/HgO} + 0.0591pH$,

where $V_{Hg/HgO}$ is the measured potential vs. alkaline Hg/HgO, $V^o_{Hg/HgO}$ is the formal potential of a standard alkaline Hg/HgO (1 M KOH) electrode. The electrolyte was purged with a gas mixture for 10 min prior to use. The electrochemical cell was made from Pyrex with a quartz window. A SP-300 Biologic potentiostat was used to control the potentials and record the data. The electrodes were illuminated using a laser-driven Xe lamp ($\lambda = 170 \sim 800$ nm). A schematic diagram of the electrochemical cell is shown

in Figure S33. The incident light intensity was controlled by a neutral density filter. For measuring light-intensity thresholds, the current density vs. light intensity was recorded. At zero current density, the corresponding light intensity is defined as the light intensity threshold. The electrochemical H_2 evolution activities of FTO/Pt and FTO/$RhCrO_x$ were measured in pure H_2 flow. For all OCP measurements, the error bars were ± 2 mV.

8. Photocatalytic water splitting activity measurements. Water splitting reaction using photocatalyst particles were carried out in a top-irradiation-type reaction cell, which was connected to a closed gas-circulation system. Photocatalysts (0.1 g) were dispersed in a 100 mL deionized water (for overall water splitting) or in a 20 vol% methanol aqueous solution (for H_2 evolution half-reactions) using ultrasonication. Prior to carrying out the reactions, the cell was evacuated to remove air and dissolved O_2 in water. The solution was then illuminated using a 300 W Xe lamp equipped with an all-reflection mirror ($\lambda > 300$ nm). The gas products were analysed by a gas chromatograph (Shimadzu, GC-8A) equipped with a thermal conductivity detector. Ar was used as a carrier gas. The reactor was water-cooled at around 15 °C during the water-splitting reactions.

9. Characterizations of materials. The crystal structures were confirmed by XRD using a Rigaku SmartLab X-ray Diffractometer in a grazing incident mode, i.e., at ω = 0.45° and with 2θ between 20 – 70 °. The morphology of the Pt particles, deposited on single crystal $SrTiO_3$, was characterized by a Bruker Dimension Fast Scan Atomic Force Microscope (AFM). A peak force tapping mode and standard AFM tips were used. A Hitachi SU8230 UHR Cold Field Emission SEM was used to characterize the cross-section and surface morphologies of Ti/$SrTiO_3$:Al and Ta/Ta_3N_5 electrodes.

10. Glossary

The Principle of Detailed Balance: This principle is essentially the same principle which has been used in detailed balance limit for calculating solar cell efficiencies. This principle here is used to account for all of the possible charge-transfer pathways across the semiconductor/water junction by invoking microscopic reversibility of kinetic rates, hence is distinctive to the context of electron-hole pair generation and recombination in calculating the Shockley-Queisser limit for solar cells.

Equilibrium: This condition only applies to “in the dark” and “in the absence of a net

current flow", which is irrelevant to photocatalysts suspended in a non-equilibrium solution with ($H_2 + O_2$) gas mixture; the semiconductor/co-catalyst solid-solid junction may equilibrate their electrochemical potentials, despite the co-catalyst may reach a steady-state potential with a non-equilibrium solution with ($H_2 + O_2$) gas mixture.

Steady State: This condition applies to both in the dark and under illumination when current density and voltage become independent of time, including non-zero net currents; this condition refers to the various scenarios of reaching a steady-state potential and net current density when in contact with a non-equilibrium solution with gas mixture.

(Net) Current Density: Whereas not explicitly mentioned, current density refers to the net current density, i.e., the arithmetic sum of both forward and backward current densities at a specific site.

Forward Current Density: A local current density resulting from transfer of electrons or holes from semiconductors to electrolytes.

Backward Current Density: A local current density resulting from extraction of electrons or holes from electrolytes back to semiconductors.

Interfacial (Total) Current Density: Arithmetic sum of both forward and backward current densities by integrating over all the locations across the liquid-junction interface

Exchange Current: The absolute value of forward or backward currents at zero net current density locally."

Supplementary Discussion

S1 Kinetic model of $SrTiO_3$/one-redox liquid junctions

A schematic for a liquid contact between n-type $SrTiO_3$ and a solution containing a redox couple, A/A^-, is shown in Figure S1. In the dark, there will be a net flow of electrons from $SrTiO_3$ to the solution redox, A/A^- (Figure S1a). The net interfacial electron current density can be expressed as

$$J_{\mathrm{n}} = -qk_{\mathrm{n}}[\mathrm{A}](n_{\mathrm{s}} - n_{\mathrm{sA}}) = -q\ k_{\mathrm{n}}[\mathrm{A}]n_{\mathrm{s0}}\{\exp[q(E_0 - E)/k_{\mathrm{B}}T] - \exp[q(E_0 - E(\mathrm{A/A^-}))/k_{\mathrm{B}}T]\} \quad \text{(S1)}$$

where k_n denotes the rate constant for electron transfer from the conduction band (CB) edge of $SrTiO_3$ to the acceptor species A; E, E_0 and $E(A/A^-)$ denote the potential of $SrTiO_3$, the flat band potential of $SrTiO_3$ and the potential of A/A^- redox, respectively; n_s, n_{s0} and n_{sA} denote the surface electron concentrations at the respective potentials of E, E_0 and $E_{A/A-}$.When the $E = E(A/A^-)$ (Figure S1b), according to the principle of microscopic reversibility, the net electron current density from $SrTiO_3$ to the solution equals to zero:

$$J_{\mathrm{n}} = 0 \text{ at } E = E(\mathrm{A/A^-}) \quad \text{(S2)}$$

In this case, the difference of electrochemical potentials between semiconductors and liquids at the liquid interface is dropped across the semiconductor. When no surface states exist on the semiconductor, its band edges are fixed relative to the redox potentials in an aqueous electrolyte.[8]

When $SrTiO_3$ is excited by UV illumination, holes will be generated in its valence band (VB). The hole concentration is determined by the local optical generation rates and the hole-transfer rate. The electron and hole quasi-Fermi levels will split (Figure S1c). The net hole current density can be expressed as

$$J_{\mathrm{p}} = qk_{\mathrm{h}}[\mathrm{A^-}](p_{\mathrm{s}} - p_{\mathrm{sA}}) \quad \text{(S3)}$$

where k_h denotes the rate constant for photo-generated holes to inject to species A^- from the VB edge; p_s denotes the averaged surface hole concentration which injects to A^- from the VB edge, p_{sA} denotes the averaged surface hole concentrations at $E(A/A^-)$. Under open-circuit conditions, the hole quasi-Fermi level equilibrates with $E(A/A^-)$ and the electron quasi-Fermi level shifts negatively to E_{OCP} where zero net charge flow passes across $SrTiO_3$/liquid junctions (Figure S1c). Under steady-state open circuits, the mathematical relationship between the net electron current density (J_n) and the net hole current density (J_p) can be described by

$$J_{\mathrm{n}} + J_{\mathrm{p}} = 0 \quad \text{(S4)}$$

S2 Energetics of a $SrTiO_3$/Pt junction in water

$SrTiO_3$/Pt may form a buried junction with fixed barrier heights, or form a $SrTiO_3$/Pt/liquid junction with variable Pt particle electrochemical potentials and variable barrier heights (adaptive junction behaviour).[9] In the buried junction limit as illustrated in Figures S2a and S2b, any potential drop at the Pt/water interface shifts the $SrTiO_3$ band edge positions by the same amount. The band bending in $SrTiO_3$ is determined by the fixed barrier height of the $SrTiO_3$/Pt Schottky junction. In the adaptive junction case as illustrated in Figures S2c and S2d, the electrochemical potential of Pt particles is determined by the kinetic branching ratios and reaches a steady-state potential in a way that can affect local band bending as Pt potentials vary, e.g., by forming surface hydrides/oxides/hydroxide/oxyhydroxides. The adaptive junction characteristic is the likely scenario as discussed in Section 5: the barrier height of local $SrTiO_3$/Pt junctions is determined by the branching ratios of charge-transfer kinetics from $SrTiO_3$ CB through Pt co-catalysts to the H^+/H_2 redox vs. to the O_2/H_2O redox, and by the local electron quasi-Fermi level. The potential of Pt particles is assumed not to affect the band edges of $SrTiO_3$, due to the adaptive junction assumption and the pinch-off effect by $SrTiO_3$/liquid junctions (Pt particle is ~ 3 nm in thickness and ~ 15 nm in radius as shown in Figure S3.).

To confirm that the $SrTiO_3$/Pt in water operates under the limit of an adaptive junction, we did the following calculation to compare the thermionic emission exchange current density across a $SrTiO_3$/Pt junction (J_{TE}) and the current density across a Pt/water junction for H_2 oxidation and O_2 reduction (J_{PW}).

The thermionic emission exchange current density between $SrTiO_3$ and Pt under equilibrium, J_{TE}, can be expressed as[10]

$$J_{TE} = A^* T^2 \exp(-q\Phi_B / k_B T) \quad \text{(S5)}$$

where A^* is a temperature-independent pre-factor indicative of the thermionic emission rate for charge transfer between $SrTiO_3$ and Pt, Φ_B is the barrier height of the junction. The flat band potential of $SrTiO_3$ is about − 0.15 V vs. RHE, so Φ_B is equal to (the potential of Pt vs. RHE + 0.15) V. A^* can be estimated by

$$A^* = 4\pi q m^* k_B^{\ 2} / h^3 \quad \text{(S6)}$$

where m^* is the electron effective mass, and h is Planck's constant. The value of m_e^* can be obtained by

$$N_c = 2(2\pi m^* k_B T / h^2)^{3/2} \quad \text{(S7)}$$

Where N_c is the effective density of states of the conduction band. For $SrTiO_3$, N_c

equals to 7.94×10^{20} cm^{-3}.[11] The value of m^* was calculated to be 9.17×10^{-30} kg. The value of A^* was calculated to be 1208.62 A·cm^{-2} K^{-2}. Based on Equation (S5), the thermionic emission exchange current J_{TE} vs. the variable potential of Pt can be obtained. This relationship was converted to J_{TE} vs. ($H_2 + O_2$) gas mixture composition as plotted in Figure S4.

The current density across a Pt/water junction for H_2 oxidation and O_2 reduction, J_{PW}, is obtained by summing the exchange current density for H_2 oxidation (i_{HOR}) and O_2 reduction (i_{ORR}) under gas mixture of various compositions.

$$J_{PW} = i_{HOR} + i_{ORR} \quad \text{(S8)}$$

$$i_{HOR} = qk_{HOR}[H_{ad}] \quad \text{(S9)}$$

$$i_{ORR} = qk_{ORR}[O_{2(ad)}] \quad \text{(S10)}$$

In pure H_2, i_{HOR} equals to the exchange current density between Pt and H^+/H_2 couple, 1.07 mA cm^{-2}; in pure O_2, i_{ORR} equals to the exchange current density between Pt and O_2/H_2O couple, 0.36 mA cm^{-2}. (derived from Figure S27)

When Pt potentials reach steady-state in a ($H_2 + O_2$) gas mixture, we can obtain:

$$qk_{HOR}[H_{ad}]e^{\frac{\alpha F \eta_{HOR}}{RT}} = qk_{ORR}[O_{2(ad)}]e^{\frac{\alpha' F \eta_{ORR}}{RT}} \quad \text{(S11)}$$

where k_{HOR} and k_{ORR} are the rate constants for H_2 oxidation and O_2 reduction, respectively ($k_{HOR}/k_{ORR} = 1.07/0.36 = 3$); α and α' are the electron transfer coefficient for H_2 oxidation and O_2 reduction, respectively, taken as 0.5. η_{HOR} and η_{ORR} are the overpotentials of hydrogen oxidation reaction and oxygen reduction reaction, respectively. η_{HOR} and η_{ORR} can be obtained by referring to the steady-state potentials of Pt particles under various ($H_2 + O_2$) gas mixture (Figure S11). Based on Equation (S11), [H_{ad}] and [$O_{2(ad)}$] under gas mixture of various compositions can be obtained. Plugging [H_{ad}] and [$O_{2(ad)}$] into Equations (S8) – (S10) gives the the value of J_{PW}. J_{PW} vs. ($H_2 + O_2$) gas mixture composition was plotted in Figure S4.

As shown in Figure S4, J_{TE} was larger than J_{PW} when the H_2 concentration > 30% in the gas mixture. In this condition, electrons transfer to Pt from the $SrTiO_3$ CB states are likely to accumulate at the Pt sites. The Fermi level of $SrTiO_3$ aligns with the poised potential of Pt where H_2 oxidation via Pt and O_2 reduction via Pt reach detailed balance in the dark. Under illumination, the potential of $SrTiO_3$ shift to be more negative than $E(H^+/H_2)$ regardless of the gas mixture composition, not the same as the potential in the

dark. In this condition, photo-generated electrons accumulate on Pt due since $J_{TE} >> J_{PW}$. The potential of Pt shifts with the electron quasi-Fermi level of $SrTiO_3$. The $SrTiO_3$/Pt junction in water operates under the limit of an adaptive junction as shown in Figure S5.

S3 Steady-state potential of $SrTiO_3$/Pt contacting a O_2/H_2O couple in aqueous solution

Semiconductor does not take on the solution redox potential but a mixed potential when another surface carrier transport occurs and the kinetics of charge transfer to solution redox is not overwhelming. When $SrTiO_3$/Pt is contacting a O_2/H_2O couple in aqueous solution, O_2 reduction (Equation (S12)) and Pt oxidation (Equation (S13)) occur:

$$4e^- + O_2 + 4H^+ \rightarrow 2H_2O \text{, } E_{O2/H2O} = 1.23 \text{ V vs. RHE (S12)}$$

$$Pt + 2OH^- \rightarrow PtO + H_2O + 2e^- \text{, } E_{PtO/Pt} = 0.88 \text{ V (S13)}$$

As a result, $SrTiO_3$/Pt will not show a steady-state potential of 1.23 V vs. RHE. The obtained potential will be a mixed value of $E_{O2/H2}$ and $E_{PtO/Pt}$. Referring to a previous study,[12] we derived the mixed potential was derived as follows.

For Pt oxidation, the oxidation current density-overpotential relationship is given by

$$J_{PtO/Pt} = i^o_{PtO/Pt}(e^{n_{PtO/Pt}\alpha_{PtO/Pt}F\eta_{PtO/Pt}/RT} - e^{-n_{PtO/Pt}(1-\alpha_{PtO/Pt})F\eta_{PtO/Pt}/RT}) \text{ (S14)}$$

where $J_{PtO/Pt}$ is the Pt oxidation current density, $i^o_{PtO/Pt}$ is the exchange current density of Pt oxidation, $n_{PtO/Pt}$ is the apparent electron transfer number in the electrochemical reaction, $\alpha_{PtO/Pt}$ is the electron transfer coefficient, and $\eta_{PtO/Pt}$ is the overpotential. Supposing that the steady-state potential of $SrTiO_3$/Pt is E_{mixed}, $\eta_{PtO/Pt} = E_{mixed} - E_{PtO/Pt}$. Assuming $\eta_{PtO/Pt}$ is larger than 0.1 V, Equation (S14) can be approximated as follows:

$$J_{PtO/Pt} = i^o_{PtO/Pt} e^{n_{PtO/Pt}\alpha_{PtO/Pt}F(E_{mixed}-E_{PtO/Pt})/RT} \text{ (S15)}$$

For O_2 reduction on Pt, a similar equation can be obtained:

$$J_{O2/H2O} = i^o_{O2/H2O} e^{n_{O2/H2O}\alpha_{O2/H2O}F(E_{O2/H2O}-E_{mixed})/RT} \text{ (S16)}$$

where $J_{O2/H2O}$ is the O_2 reduction current density, $i^o_{O2/H2O}$ is the exchange current density of O_2 reduction, $n_{O2/H2O}$ is the apparent electron transfer number in the electrochemical reaction, $\alpha_{O2/H2O}$ is the electron transfer coefficient.

At a steady-state condition, no net current density is flowing through $SrTiO_3$/Pt, e.g. $J_{PtO/Pt} = J_{O2/H2O}$. Thus,

$$i^o_{PtO/Pt} e^{n_{PtO/Pt}\alpha_{PtO/Pt}F(E_{mixed}-E_{PtO/Pt})/RT} = i^o_{O2/H2O} e^{n_{O2/H2O}\alpha_{O2/H2O}F(E_{O2/H2O}-E_{mixed})/RT} \text{ (S17)}$$

Assuming the exchange current density, apparent electron transfer number and the electron transfer coefficient are the same for both O_2 reduction and Pt oxidation, the value of E_{mixed} (= 1.06 V) can be obtained by Equation (S17). Note that E_{mixed} depends

on the chemical status of Pt, such as the coverage of PtO on Pt.

S4 Light intensity dependence of $SrTiO_3$/co-catalyst/water junctions

We expect to see a light-intensity threshold when a liquid-junction interface involves multiple electron-transfer pathways (see Section 2.3). One of these pathways may result in H_2 and O_2 recombination. Therefore, a finite light-intensity threshold is required to reach a net zero current under illumination. To verify this point, a three-electrode cell (illustrated in Figure S7) was adapted to simulate a two-electrode water-splitting cell and to measure the light-intensity-dependent photocurrents. Herein, a $SrTiO_3$/Pt and a $SrTiO_3$/(Cr_2O_3/Pt) photoelectrode were used as the working electrodes with its back-contact potential fixed at 0 V vs. RHE. The 0 V vs. RHE potential set the working electrode as if it were to operate in a two-electrode water-splitting cell, where the H_2-evolving counter electrode would operate at approximately the standard potential of H^+/H_2 couples.[13] If pure O_2 gas were used to purge the solution, the working electrode would inject electrons to both H^+/H_2 and O_2/H_2O couples simultaneously, as operating photocatalysts. Instead, if pure H_2 gas were used to purge the electrolyte, O_2 was not available for electron transfer. Therefore, a light-intensity threshold should be observed in a H_2/O_2 mixture but not in pure H_2. Alternatively, Cr_2O_3 would create kinetic-controlled selectivity for Pt and supress its O_2 reduction.

The current density with the $SrTiO_3$ back contact poised at 0 V vs. RHE as a function of light intensity ($\lambda < 390$ nm) was shown in Figure S8. The light-intensity threshold for $SrTiO_3$/Pt in O_2 purged electrolyte was measured as 200 $mW \cdot cm^{-2}$. The H_2/O_2 recombination current for $SrTiO_3$/Pt in O_2 was 0.089 $mA \cdot cm^{-2}$, which existed irrespective of the light intensity. The existence of a light-intensity threshold suggests that H_2 generation induced by photon flux must overcome H_2 consumption for achieving net H_2 accumulation during water splitting. Otherwise, the $SrTiO_3$/Pt/water junction would only recombine H_2 and O_2 via backward electron transfer from H_2.

Compared with $SrTiO_3$/Pt in O_2 purged electrolyte, $SrTiO_3$/(Cr_2O_3/Pt) showed a lower recombination current density of 0.015 $mA \cdot cm^{-2}$ and a lower light intensity threshold at 160 $mW \cdot cm^{-2}$. The Cr_2O_3 layer on Pt effectively supressed the electron-transfer pathway to O_2/H_2O. The $SrTiO_3$/(Cr_2O_3/Pt) electrode at 0 V vs. RHE should show zero dark current and no light intensity threshold if electron-transfer selectivity to H^+/H_2 were 100%. The slight discrepancy was likely because without a well-defined

482 H^+/H_2 couple in O_2 purged electrolyte, electrons mainly transferred to surface defects
483 or spurious intermediates, such as CrO_4^{2-} species.
484 $SrTiO_3$/Pt in H_2 purged electrolyte completely shut the electron-transfer pathway
485 to O_2. There would be no H_2 and O_2 recombination, and therefore no light-intensity
486 threshold was observed, as reflected in Figure S8. In this cell, the electrons either
487 injected to H^+/H_2 to make Pt-H or transported across $SrTiO_3$ photocatalysts to its back
488 contacts at 0 V vs. RHE. Clearly, a light-intensity threshold may not exist for
489 semiconductor/two-redox liquid junctions. These observations supported the
490 fundamental principle of detailed balance--the net rates of all forward and backward
491 charge-transfer fluxes determine the current-potential behaviour of
492 semiconductor/liquid junctions.

493 **S5 Band structures of single-crystalline $SrTiO_3$**

494 The CB minimum and VB maximum of single-crystalline $SrTiO_3$ photoelectrodes
495 have previously been measured to be − 0.4 V and 2.9 V vs. RHE, respectively,[14] and
496 flat band potential was estimated by OCP measurements under illumination as shown
497 in Figure S9. As the light intensity continued to increase, the OCP continued to decrease
498 and reached a steady-state value at −0.15 V vs. RHE, which is assigned as its flat band
499 potential. According to the experimental results and previous studies,[14, 15] the band
500 diagram of the n-type single-crystalline $SrTiO_3$ in vacuum was depicted in Figure S10.
501
502

503 **S6 Charge transfer at $SrTiO_3$/water junctions in the dark**

504 As shown in Figure 3a, the OCP transient from light to dark took about 1000 s for
505 bare $SrTiO_3$, due to slow electron-transfer kinetics over its surface. Even with a pure
506 O_2 flow, the OCP was 0.57 V vs. RHE, still 0.49 V more negative than 1.06 V vs. RHE.
507 Even in pure H_2 flow, the OCP was 0.44 V vs. RHE, still 0.44 V more positive than 0
508 V vs. RHE. As discussed in Section 2.3, the OCPs (in the potential scale) of an ideal
509 semiconductor/water junction in the dark should be close to 0 V vs. RHE under a 100%
510 H_2 flow, and close to 1.06 V vs. RHE under a 100% O_2 gas flow. However, the
511 measured OCPs were insensitive to the gas compositions, remaining almost half-way
512 between 0 and 1.06 V vs. RHE. One reason to explain this observation could be the
513 slow kinetics of any forward/backward charge-transfer pathways to either of the redox
514 potentials. Another factor could be that the surface states on bare $SrTiO_3$ dominated
515 electron transfer at the $SrTiO_3$/water junction. A previous study reported that the surface
516 states of $SrTiO_3$ due to the formation of Ti^{3+} or oxygen vacancy were located at ca. 0.6

V vs. RHE.[16] The presence of these surface states might result in the measured OCP range of 0.44 to 0.57 V vs. RHE.

S7 Electron-transfer kinetics at a $SrTiO_3$/Pt/water junction under a flow of (H_2 + N_2) or (O_2 + N_2) mixture

The OCPs of $SrTiO_3$/Pt in water under a (H_2 + N_2) or a (O_2 + N_2) gas mixture were shown in Figure S12a and S12b, respectively. The difference of OCPs in the dark under a (100% H_2 + 0% N_2) vs. a (20% H_2 + 80% N_2) gas mixture was 80 ± 4 mV, which was slightly larger than the formal potential shift of 41 mV caused by diluting pure H_2 to 20%. A similar result was also observed when pure O_2 was diluted to 20% by N_2. In this case, the difference in OCP was 154 ± 4 mV, also larger than the formal potential shift. These results indicate that other electron transfer pathways, possible to surface states, were concomitant with electron transfer to H^+/H_2 and O_2/H_2O redox. The electron-transfer rate to surface states were compared with those to H^+/H_2 and to O_2/H_2O in the following paragraphs.

The OCP of $SrTiO_3$/Pt in the dark in pure H_2 was estimated to be 20 ± 2 mV vs. $E(H^+/H_2)$, as shown in Figure 3b. The OCPs of Pt/$SrTiO_3$ in the dark in pure N_2 was measured to 240 ± 2 mV vs. $E(H^+/H_2)$ as shown in Figure S12. When Pt/$SrTiO_3$ was purged with N_2, only the surface states were available to trap electrons from $SrTiO_3$/Pt. Consequently, the dark OCP at 100% N_2 is assumed to be the potential of surface states. Based on the rate law of steady-state equilibrium in the dark, we can deduce,

$$J_{H^+/H_2} + J_{ss} = 0 \quad \text{(S18)}$$

where $J_{H+/H2}$ and are J_{ss} the current density from $SrTiO_3$ to H^+/H_2 and surface states, respectively, at OCP of $SrTiO_3$/Pt in the dark in pure H_2. Based on the principle of detailed balance,

$$J_{H^+/H_2} = j_1 \exp[(0-20)\text{mV}/(k_B T/q)] - j_1 \quad \text{(S19)}$$

where J_1 is the exchange current density between $SrTiO_3$/Pt and H^+/H_2;

$$J_{ss} = j_2 \exp[(240-20)\text{mV}/(k_B T/q)] - j_2 \quad \text{(S20)}$$

where j_2 is the exchange current density between $SrTiO_3$/Pt and surface states. According to Equation (S18), j_2 is four orders of magnitude lower than j_1. Therefore, the electron-transfer rate between $SrTiO_3$/Pt and surface states is minor compared to that between $SrTiO_3$/Pt and H^+/H_2. Such an estimation is equally applicable to the OCP behaviour under a (O_2 + N_2) mixture.

S8 Quantitative fitting for the kinetic rate law of the forward electron transfer from $SrTiO_3$/Pt to O_2/H_2O

S8.1 Extracting $J_{2,forward}$ from J

Figure S14 shows the Log$J$ vs. E curves for $SrTiO_3$/Pt under various compositions of (H_2 + O_2) gas mixtures. In the measurement, E was scanned from the OCP in the dark to slightly more positive than $E(H^+/H_2)$ (i.e. 0 V vs. RHE).

According to Equation (18), the net current density across the $SrTiO_3$/Pt/water junction at steady-state condition should be zero, i.e. detailed balance. Under OCP conditions in the dark, $J_{1,\text{forward}}$ and $J_{2,\text{backward}}$ are negligible. Therefore, Equation (18) can be expressed as

$$J_{1,\text{backward}} + J_{2,\text{forward}} = 0 \quad \text{(S21)}$$

$$qk_1[\text{Pt}^*]n_{s0}\exp[q(E_0 - E_1)/n_1k_BT] - qk_2[\text{O}_{2(\text{ad})}]n_{s0}\exp[q(E_0 - E)/n_2k_BT] = 0 \quad \text{(S22)}$$

Taking E as the OCPs of $SrTiO_3$/Pt electrodes in the dark at steady-state condition (summarized in Table S1) and plugging E into Equation (S22) gives us pre-factor ratios of $k_1[\text{Pt}^*]/k_2[\text{O}_{2(\text{ad})}]$ under various gas compositions (summarized in Table S2). Note that the (100% O_2 + 0% H_2) and (100% H_2 + 0% O_2) were excluded from the table since H^+/H_2 and O_2/H_2O do not have a well-defined potential in the electrolyte in these cases. With the values of $k_1[\text{Pt}^*]/k_2[\text{O}_{2(\text{ad})}]$, the ratios between $J_{1,\text{backward}}$ and $J_{2,\text{forward}}$ at each applied potential can be confirmed. For example, in a (60% O_2 + 40% H_2) gas mixture, $k_1[\text{Pt}^*]/k_2[\text{O}_{2(\text{ad})}] = 3.81 \times 10^{-9}$, and $|J_{1,\text{ backward}}| << |J_{2,\text{ forward}}|$ when $E < 0.2$ V vs. RHE. Based on the ratios between $J_{1,\text{backward}}$ and $J_{2,\text{forward}}$ at each applied potential under various gas compositions, log$J_{2,\text{forward}}$ vs. ($E_0 - E$) curve (Figure S15) was extrapolated from Figure S14.

Table S1. OCPs of $SrTiO_3$/Pt electrodes in the dark at steady-state condition under various gas compositions

Gas mixture composition	OCP / V vs. RHE
80% O_2 + 20% H_2	0.560
60% O_2 + 40% H_2	0.498
40% O_2 + 60% H_2	0.423
20% O_2 + 80% H_2	0.328

Table S2. Ratios between pre-factors, $k_1[\text{Pt}^*]/k_2[\text{O}_{2(\text{ad})}]$

Gas mixture composition	$k_1[Pt^*]/k_2[O_{2(ad)}]$
80% O_2 + 20% H_2	3.41×10^{-10}
60% O_2 + 40% H_2	3.81×10^{-9}
40% O_2 + 60% H_2	7.05×10^{-8}
20% O_2 + 80% H_2	2.85×10^{-6}

S8.2 Log-linear fitting of $J_{2,forward}$

As shown in Figure S16, the $\log J_{2,\text{forward}}$ vs. $(E_0 - E)$ curves were linear in a certain region. The slopes of these curves at the linear region at various (H_2 + O_2) gas mixtures were fitted. These slopes were fitted to be 157 - 167 mV dec^{-1}, which is consistent with Tafel slope of ORR on Pt.[17] These fitting results validated the exponential term, $\exp[q(E_0 - E)/n_2k_BT]$, in Equation (10). Furthermore, they validated our adaptive junction assumption, where the charge transfer between Pt and water limits the charge transfer at a $SrTiO_3$/Pt/water junction.

The logarithm of the pre-factor, $qk_2[O_{2(ad)}]n_{s0}$, of Equation (10) is equal to the intercept of the linear fitting line with the $\log J_{2,\text{forward}}$ axis. The values of $qk_2[O_{2(ad)}]n_{s0}$ were obtained as shown in Table S3. The values will be compared with those calculated based on the detailed balance of electron transfer in the dark in a (O_2 + N_2) gas mixture. Here, we assume that the pre-factor is only dependent on the O_2 concentration in a gas mixture. The OCPs of $SrTiO_3$/Pt electrodes in the dark at steady-state condition in a (O_2 + N_2) gas mixture were summarized in Table S4. According to detailed balance, the steady-state net current density across the $SrTiO_3$/Pt/water junction should be zero. In a (O_2 + N_2) gas mixture without H_2, H^+/H_2 does not have a well-defined potential in the electrolyte: $J_{1,\text{forward}} \approx 0$ because Pt sites are mostly covered by O_2; and $J_{1,\text{backward}} \approx 0$ because $[H_{ad}]$ is negligible. Therefore, electron current density to H^+/H_2 (J_1) is negligible, i.e., $J_1 \approx 0$. J_2 is the main portion of interfacial electron current density and can be expressed as:

$$J_2 = -qk_2[O_{2(ad)}]n_{s0}\exp[q(E_0 - E)/n_2k_BT] + J_{2,\text{backward}} \quad (23)$$

At steady-state condition, $J_2 = 0$. $J_{2,\text{backward}}$ can be expressed as:

$$J_{2,\text{backward}} = qk_2[O_{2(ad)}]n_{s0}\exp[q(E_0 - E)/n_2k_BT] \quad (24)$$

$J_{2,\text{backward}}$ is a gas composition independent constant according to Equations (16). Taking E as the OCPs of $SrTiO_3$/Pt electrodes in the dark at steady-state condition (summarized in Table S4) and plugging E into Equation (S24) gave the pre-factors, i.e. $qk_2[O_{2(ad)}]n_{s0}$, at various O_2 compositions. We simply used a constant α to represent the

relative ratios for all of the pre-factors $qk_2[O_{2(ad)}]n_{s0}$, as summarized in Table S5. The values of $qk_2[O_{2(ad)}]n_{s0}$ from the two independent methods, i.e. fitting and OCP measurement, were then compared in Figure S17. Log($qk_2[O_{2(ad)}]n_{s0}$) showed similar trend in both cases, thus validating the pre-factor term, $qk_2[O_{2(ad)}]n_{s0}$, of Equation (10).

Table S3. Relative ratios of the $qk_2[O_{2(ad)}]n_{s0}$ pre-factors extracted as the intercepts

Gas mixture composition	Log($qk_2[O_{2(ad)}]n_{s0}$)
100% O_2 + 0% N_2	-1.122
80% O_2 + 20% N_2	-1.149
60% O_2 + 40% N_2	-1.185
40% O_2 + 60% N_2	-1.230
20% O_2 + 80% N_2	-1.450

Table S4. OCPs in the dark at steady-state condition in a (O_2 + N_2) gas mixture

Gas mixture composition	OCP in the dark / V vs. RHE
100% O_2 + 0% N_2	0.726
80% O_2 + 20% N_2	0.719
60% O_2 + 40% N_2	0.716
40% O_2 + 60% N_2	0.707
20% O_2 + 80% N_2	0.695

Table S5. Relative ratios of $qk_2[O_{2(ad)}]n_{s0}$ obtained based on detailed balance

Gas mixture composition	$qk_2[O_{2(ad)}]n_{s0}$	Log($qk_2[O_{2(ad)}]n_{s0}$)
100% O_2 + 0% N_2	$7.45\alpha^*$	$1.87 + \log\alpha$
80% O_2 + 20% N_2	6.19α	$1.79 + \log\alpha$
60% O_2 + 40% N_2	5.38α	$1.73 + \log\alpha$
40% O_2 + 60% N_2	3.71α	$1.57 + \log\alpha$
20% O_2 + 80% N_2	2.37α	$1.37 + \log\alpha$

$^*\alpha$ is an arbitrary constant to present the pre-factor ratios.

S9 Hole quasi-Fermi levels and estimation of photovoltages.

Different from the electron quasi-Fermi level position, the hole quasi-Fermi level position of n-type $SrTiO_3$ under illumination cannot be directly measured by OCPs. As discussed in Section 2.2, holes transfer across a $SrTiO_3$/Pt/junction only through bare $SrTiO_3$ sites. This deduction suggests that the hole quasi-Fermi level will be pinned at

626 the formal potential of OH_{ad} as a rate-determining intermediate, which is at an
627 overpotential added to the O_2/H_2O redox potential. This deduction is consistent with a
628 previous study on photoelectrochemical water oxidation using an in-situ potential
629 sensing technique for co-catalysts under operation, where their potentials were shown
630 to be (1.23 V vs. RHE + an overpotential).[18]
631 The photovoltage generated in a semiconductor/liquid junction is defined as the
632 difference between the electron quasi-Fermi level at the electron accumulation site (Pt
633 co-catalysts) and the hole quasi-Fermi level at the hole accumulation sites (bare
634 $SrTiO_3$). The photovoltage of $SrTiO_3$ should be calculated as [(1.23 V vs. RHE +
635 overpotential) – OCP under illumination vs. RHE)] instead of (OCP in the dark – OCP
636 under illumination). We found that the more negative the OCP under illumination is,
637 the higher the photovoltage is. Charge-separation efficiency is a fundamental parameter
638 that describes the portion of charge separated per total charge generated inside
639 photocatalysts. In other words, the more negative the potential of electron quasi-Fermi
640 levels, the higher the charge-separation efficiency.
641
642 **S10 Effects of back contacts on the OCP measurement of Photocatalyst Particles**
643 Ti and Ta layers are successfully used as ohmic back contacts to $SrTiO_3$:Al
644 particulate-based electrodes and Ta_3N_5 thin-film-based electrodes, respectively, for
645 direct measurement of their electron quasi-Fermi levels, and electrons are considered
646 to hop through the particle films and get collected by the back contact. The
647 electrochemical potential of a Ti layer was not sensitive to the composition of the H_2/O_2
648 mixture (shown in Figure S18). The Ta layer was fully covered by a Ta_3N_5 film and
649 isolated from the electrolyte as shown in Figure S19. Thus, its potential did not depend
650 on the composition of the H_2/O_2 mixture either.
651
652 **S11 Charge-separation and charge-transfer processes of $SrTiO_3$:Al/$RhCrO_x$ vs.**
653 **$SrTiO_3$:Al/Pt**
654 The dark OCPs of Ti/$SrTiO_3$:Al/$RhCrO_x$-particle photoelectrodes in pure H_2 and
655 O_2 were measured to be 0.26 V and 0.67 V vs. RHE, respectively, with a difference of
656 0.41 V (Figure S26a). $RhCrO_x$ does not supress O_2 reduction as much as Pt/Cr_2O_3 does.
657 This difference was higher than that of Ti/$SrTiO_3$:Al due to its pinning to surface states,
658 but noticeably lower than that of Ti/$SrTiO_3$:Al/Pt-particle photoelectrodes. The OCPs
659 also showed gas-composition dependence in a (H_2 + N_2) gas mixture (Figure S26b) or
660 a (O_2 + N_2) gas mixture (Figure S26c). These results suggested that the electron-transfer

661 pathways to the H^+/H_2 and O_2/H_2O redox couples were mainly through $RhCrO_x$ co-
662 catalysts, and that the electron-transfer pathways through surface traps on $SrTiO_3$:Al
663 was not negligible. The surface states on $SrTiO_3$:Al are either native or due to $RhCrO_x$
664 loading. Nevertheless, the water-splitting activity of $SrTiO_3$:Al/$RhCrO_x$ was about two
665 orders of magnitude higher than that of $SrTiO_3$:Al/Pt in pure H_2, by comparing data
666 shown in Figures S24 and S25. Hence, the better water-splitting performance of
667 $SrTiO_3$:Al/$RhCrO_x$ was not due to better kinetics, nor better redox selectivity, but other
668 factors.

669 To understand the functionalities of $RhCrO_x$ co-catalysts, we further compared
670 OCPs of Ti/$SrTiO_3$:Al/$RhCrO_x$ and Ti/$SrTiO_3$:Al/Pt under illumination, which
671 provided information about the respective charge separation efficiency. As shown in
672 Figure 6c, the OCPs of Ti/$SrTiO_3$:Al/$RhCrO_x$ under illumination ranged from − 0.1 to
673 − 0.2 V vs. RHE, which was about 0.2 V more negative than the OCPs of
674 Ti/$SrTiO_3$:Al/Pt under illumination for all gas compositions. The electrocatalytic H_2
675 evolution activities of Pt and $RhCrO_x$ catalysts on FTO substrates were similar, as
676 shown in Figures S27a–S27c, which suggested that their H_2-evolution kinetics were
677 comparable. The more negative OCPs for Ti/$SrTiO_3$:Al/$RhCrO_x$ under illumination can
678 be attributed to a better charge separation efficiency in $SrTiO_3$:Al/$RhCrO_x$ particles.
679 When the O_2 concentration in the gas mixture was higher than 60%, the OCPs in the
680 dark of Ti/$SrTiO_3$:Al/$RhCrO_x$ were more negative than those of Ti/$SrTiO_3$:Al/Pt (filled
681 dots in Figure 6b vs. 6c). At O_2 > 60% and H_2 < 40%, the band bending asymmetry
682 across the reductive (electron accumulation) and oxidative (hole accumulation) sites on
683 $SrTiO_3$:Al/$RhCrO_x$ particles was more favourable for charge separation than for
684 $SrTiO_3$:Al/Pt particles. The OCP measurements suggested that the charge-separation
685 efficiency at individual $SrTiO_3$:Al/$RhCrO_x$ particles was higher than $SrTiO_3$:Al/Pt
686 particles, as indicated by the consistently more negative OCPs under illumination.
687 When the O_2 concentration in the gas mixture was lower than 60%, the dark OCPs of
688 Ti/$SrTiO_3$:Al/$RhCrO_x$ became more positive than those of Ti/$SrTiO_3$:Al/Pt (filled dots
689 in Figure 6b vs. 6c). In this circumstance, the band bending in $SrTiO_3$:Al/Pt became
690 sufficiently asymmetric and became favourable for charge separation. However, the
691 OCPs of Ti/$SrTiO_3$:Al/Pt under illumination were still less negative than
692 Ti/$SrTiO_3$:Al/$RhCrO_x$, revealing less efficient charge separation on $SrTiO_3$:Al/Pt
693 particles. Our observations indicated that the charge-separation efficiency for
694 $SrTiO_3$:Al/Pt photocatalysts was deteriorated by the severe charge recombination
695 occurring at the $SrTiO_3$:Al/Pt/water interface. This negative effect of using metallic Pt

696 as a co-catalyst was also reported for GaN/Pt systems.[19] Therefore, the improved charge
697 separation at $SrTiO_3$:Al/$RhCrO_x$ particles may be due to 1) less recombination at the
698 $SrTiO_3$:Al/$RhCrO_x$ interfaces, and/or 2) significant band bending asymmetry at the
699 electron and hole accumulation sites under the full span of gas compositions, as shown
700 in Figure S28.
701

Supplementary Figures

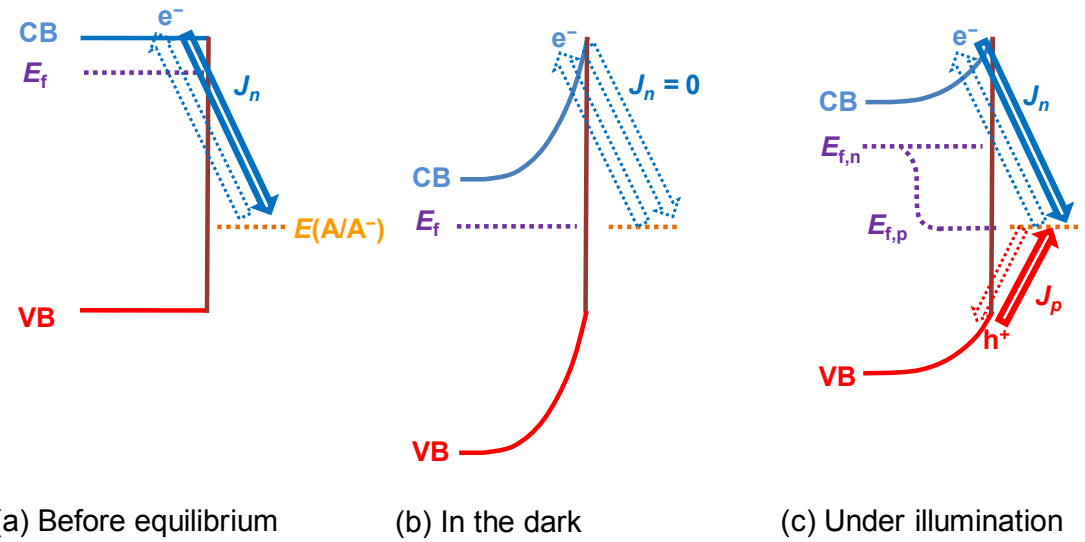

(a) Before equilibrium (b) In the dark (c) Under illumination

Figure S1. Charge-transfer process at $SrTiO_3$/one-redox liquid junctions and steady-state current-potential (J-E) behaviour of $SrTiO_3$ photoelectrodes in the dark and under illumination. E_f, $E_{f,n}$ and $E_{f,p}$ denote the potentials of the Fermi level, electron quasi-Fermi level and hole quasi-Fermi level of $SrTiO_3$, respectively; $E(A/A^-)$ denotes the redox potential of A/A^-; J_n denotes the net electron current density from $SrTiO_3$ to solution; J_p denotes the net hole current density from $SrTiO_3$ to solution. The solid arrows and dashed arrows represent the major and minor pathways for charge transfer, respectively.

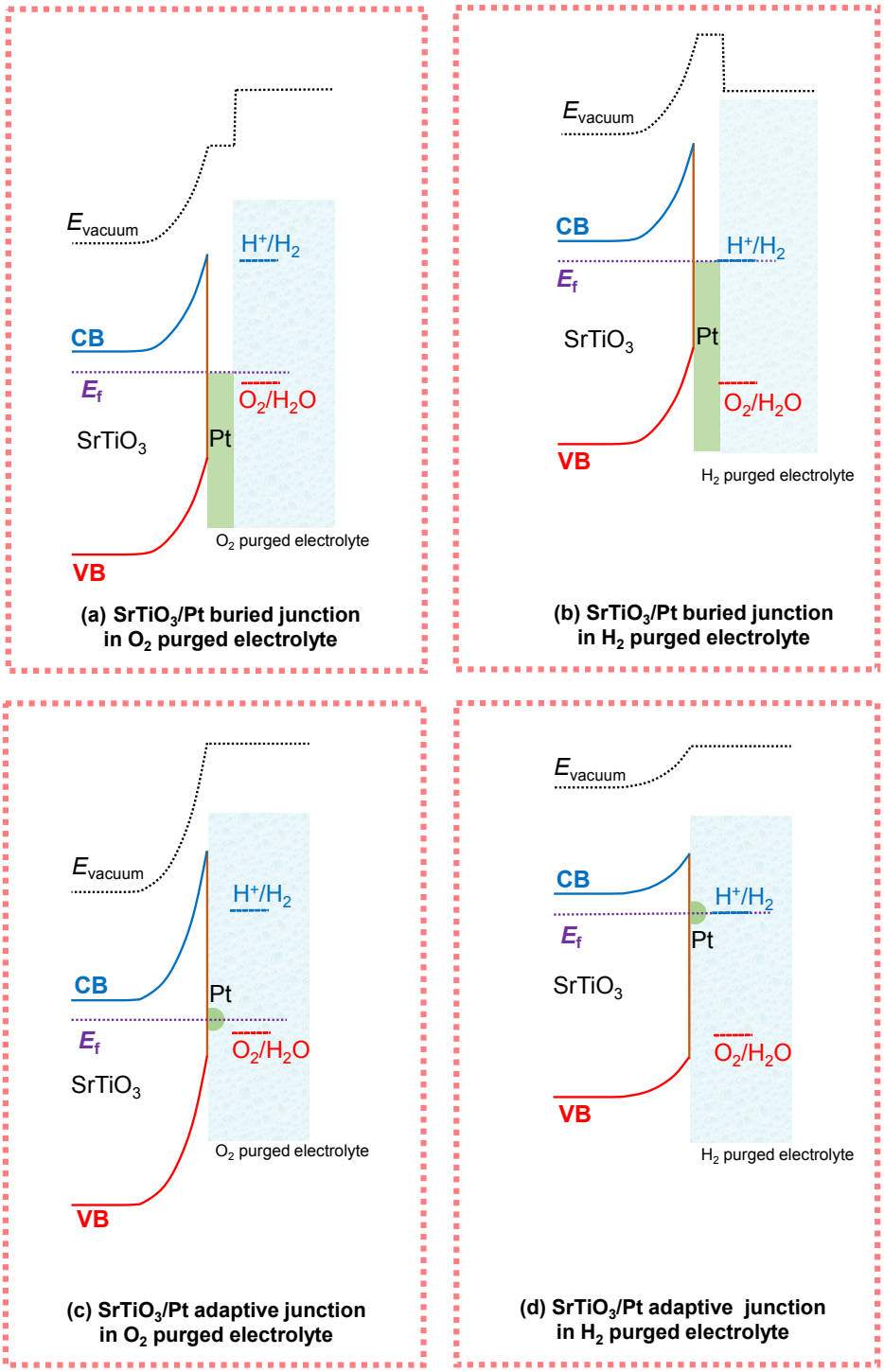

Figure S2. Postulated energy diagrams of $SrTiO_3$/Pt/water junctions in water purged by a mixture of H_2 and O_2 gases: (a) and (b) in the limit of a buried junction; (c) and (d) in the limit of an adaptive junction. The local junction energetics for (a) and (c) are drawn for O_2-purged electrolytes; and (b) and (d) for H_2-purged electrolytes.

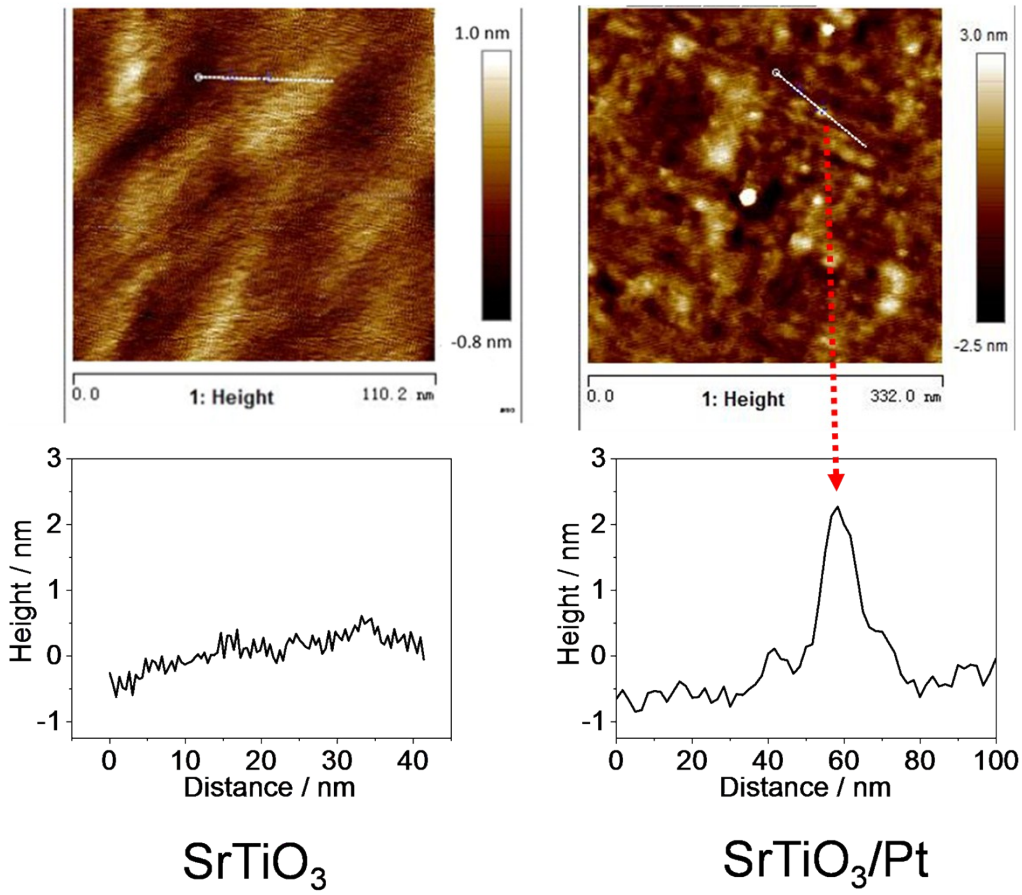

Figure S3. AFM images of bare $SrTiO_3$ and $SrTiO_3$/Pt. For the $SrTiO_3$ surface, a 110 × 110 nm^2 area was selected to represent its surface morphology, and the randomly chosen cross section (dashed white line) shows that the average surface step height is about 0.3 nm; whereas on the $SrTiO_3$/Pt surface, a representative area of 332 × 332 nm^2 was selected, and the average step height was about 1.6 nm, which indicated the deposition of Pt nanoparticles on the $SrTiO_3$ surface. The radius of Pt particles is about 15 nm and the thickness is about 3 nm.

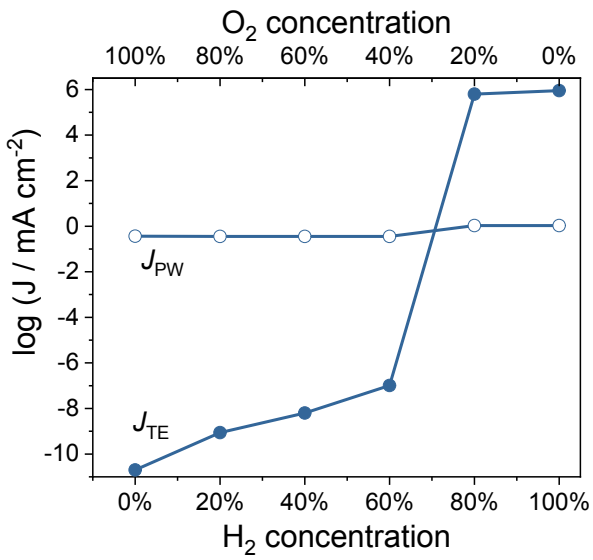

Figure S4. Log–linear plots of J_{TE} and J_{PW} vs. compositions of (H_2+ O_2) gas mixture.

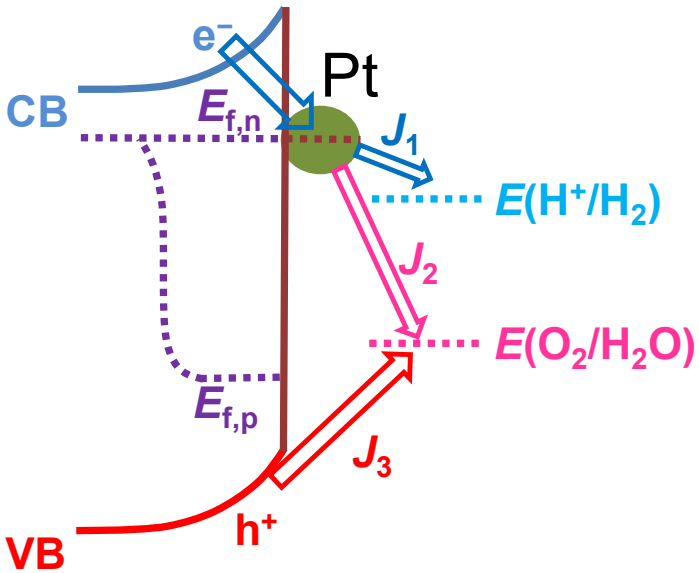

Figure S5. A proposed model for the charge-transfer process at a $SrTiO_3$/Pt/water junction under illumination. J_1 and J_2 denote the net electron current densities to H^+/H_2 and O_2/H_2O, respectively. J_3 denotes the net hole current density to O_2/H_2O. $E_{f,n}$ and $E_{f,p}$ denote the potentials of electron quasi-Fermi level and hole quasi-Fermi level of $SrTiO_3$, respectively. For each redox, the forward and reverse pathways were not shown individually but, for simplicity, were shown as an arithmetic sum of the respective forward and reverse fluxes.

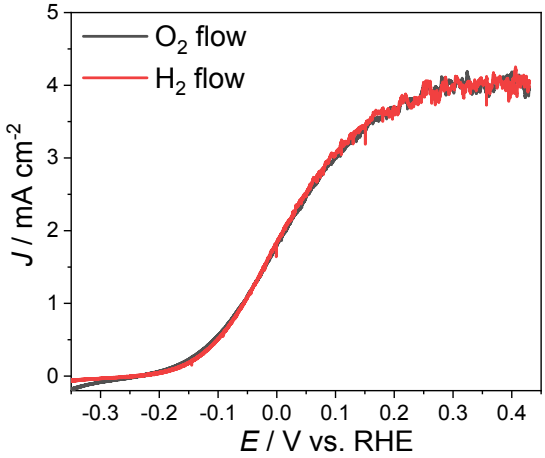

Figure S6. *J–E* curves for a single-crystalline $SrTiO_3$/Pt photoelectrode under illumination with either H_2 or O_2 flow. The electrolyte is 0.5 M Na_2SO_4(aq) solution with pH adjusted to 12.5.

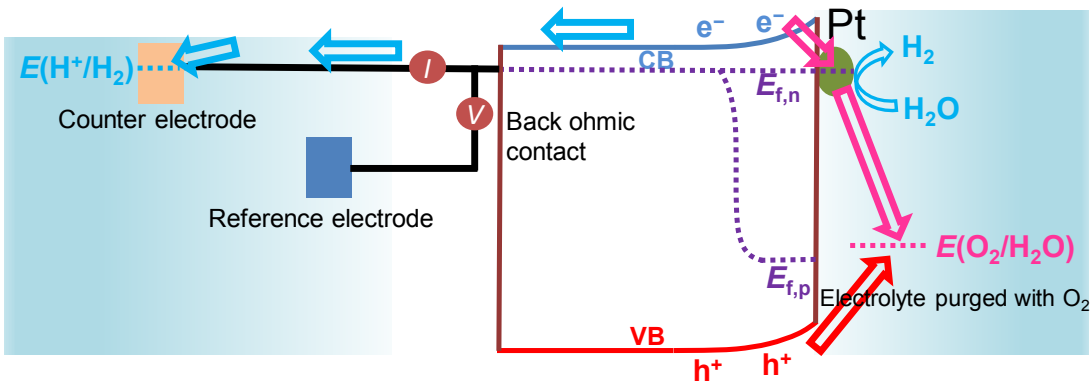

(a) Three-electrode cell purged with pure O_2

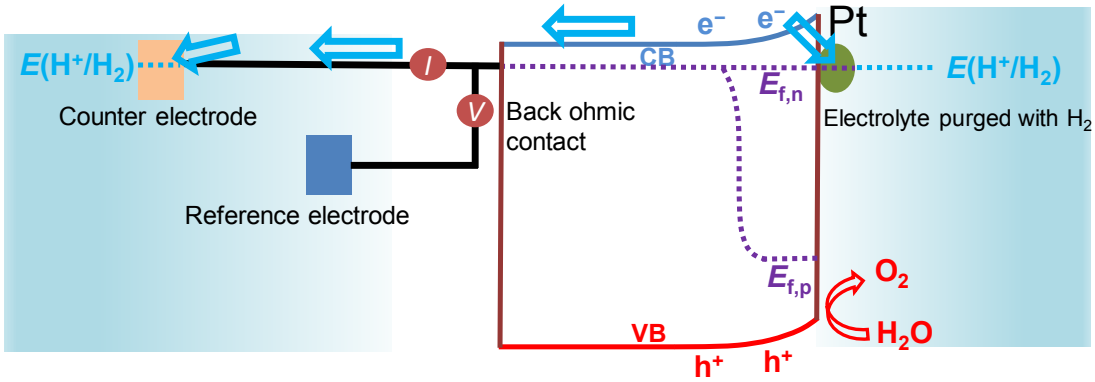

(b) Three-electrode cell purged with pure H_2

Figure S7. Schematics of a three-electrode setup purged with (a) O_2 or (b) H_2 for measuring the light-intensity dependent photocurrents. When the setup was purged with

O_2, a standard H^+/H_2 redox couple did not exist in the electrolyte. For this reason, $E(H^+/H_2)$ was not shown. When the setup was purged with H_2, a standard O_2/H_2O redox couple did not exist in the electrolyte. For this reason, $E(O_2/H_2O)$ was not shown. Arrows show H_2 or O_2 evolution that still occurs but without a well-defined potential. The potential of the electrode was poised at 0 V vs. RHE. In this figure, electron and hole quasi Fermi levels are drawn but for Pt and $SrTiO_3$ sites, respectively.

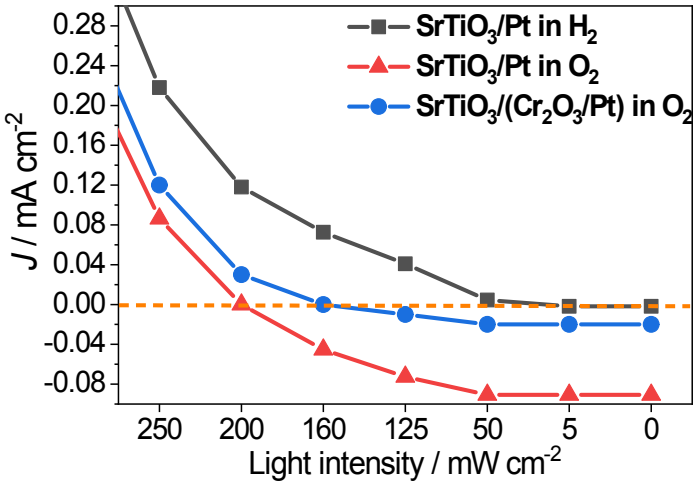

Figure S8. Current density measured at $SrTiO_3$/co-catalyst/water junctions as a function of light intensity, with the $SrTiO_3$ back contacts poised at 0 V vs. RHE. The electrolyte is 0.5 M Na_2SO_4(aq) solution with pH adjusted to 12.5.

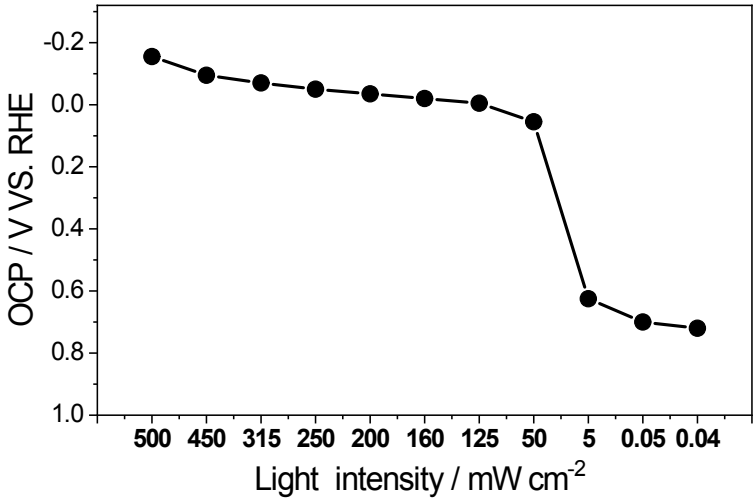

Figure S9. Open-circuit potential of single-crystalline $SrTiO_3$ as a function of illumination intensity. The electrolyte is 0.5 M Na_2SO_4(aq) solution with pH adjusted to 12.5.

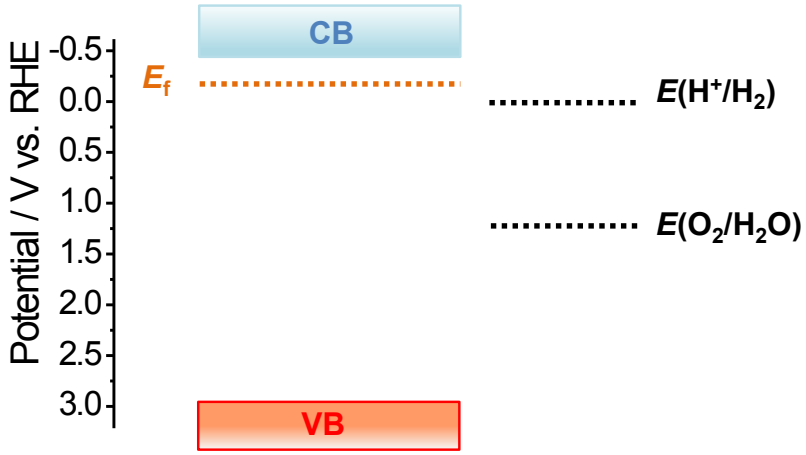

Figure S10. Energy diagram of single-crystalline $SrTiO_3$.

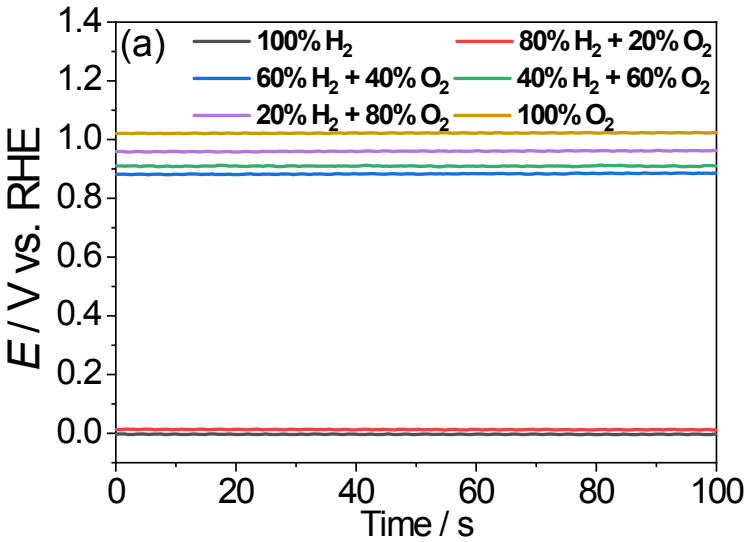

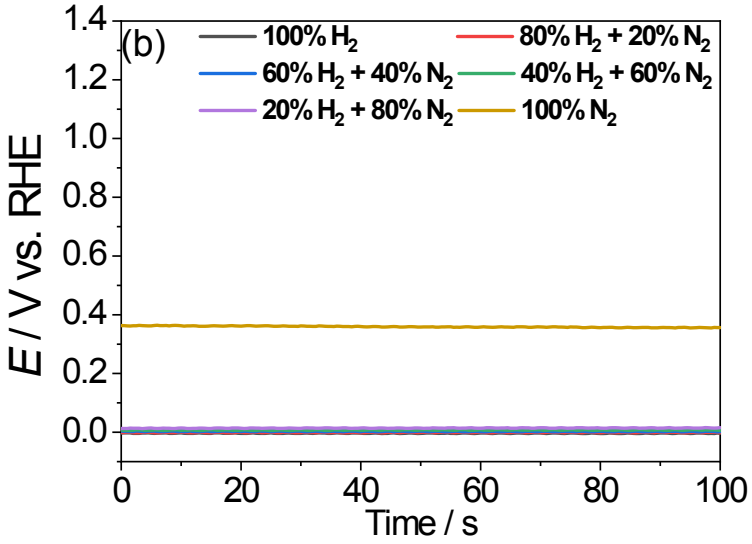

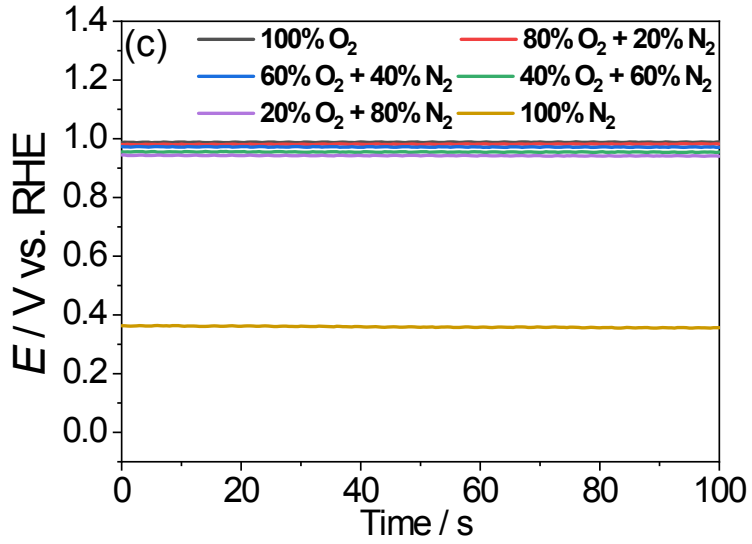

Figure S11. OCPs of an FTO/Pt electrode in an aqueous electrolyte purged with (a) a (H_2 + O_2) gas mixture, (b) a (H_2 + N_2) gas mixture or (c) a (O_2 + N_2) gas mixture. The electrolyte is 0.5 M Na_2SO_4(aq) solution with pH adjusted to 12.5.

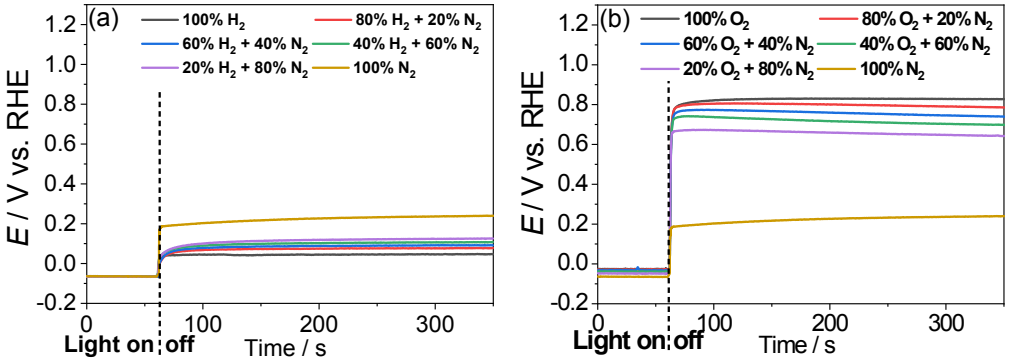

Figure S12. OCPs of a $SrTiO_3$/Pt photoelectrode in an aqueous electrolyte purged with (a) a (H_2 + N_2) gas mixture or (b) a (O_2 + N_2) gas mixture. The electrolyte is 0.5 M Na_2SO_4(aq) solution with pH adjusted to 12.5.

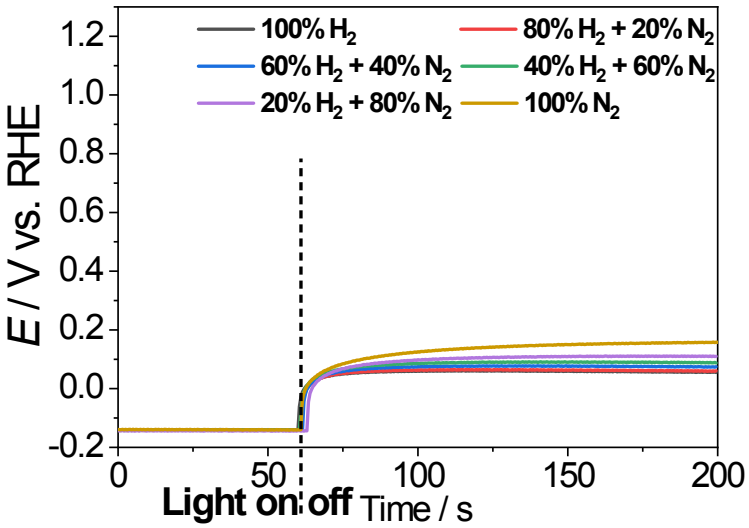

Figure S13. OCPs of a $SrTiO_3$/(Cr_2O_3/Pt) photoelectrode in an aqueous electrolyte purged with a (H_2 + N_2) gas mixture. The electrolyte is 0.5 M Na_2SO_4(aq) solution with pH adjusted to 12.5.

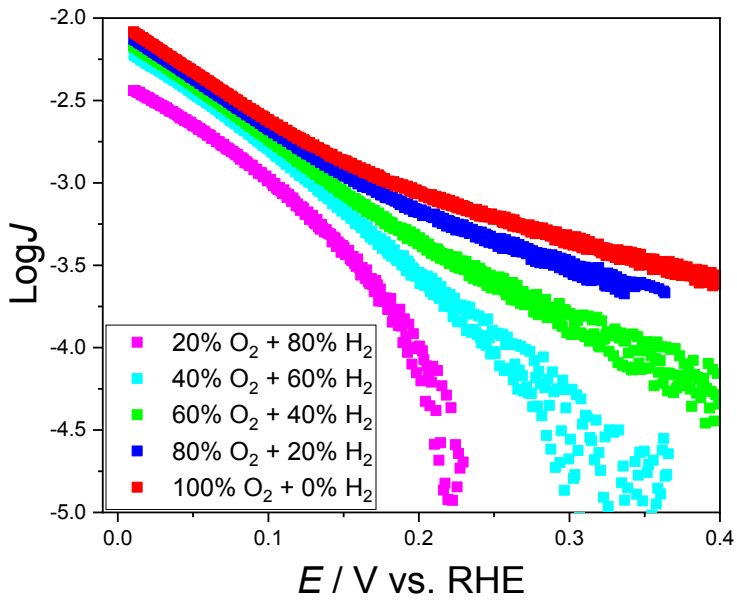

Figure S14. Log-linear plots of J vs. E for $SrTiO_3$/Pt electrodes with a (H_2 + O_2) gas mixture.

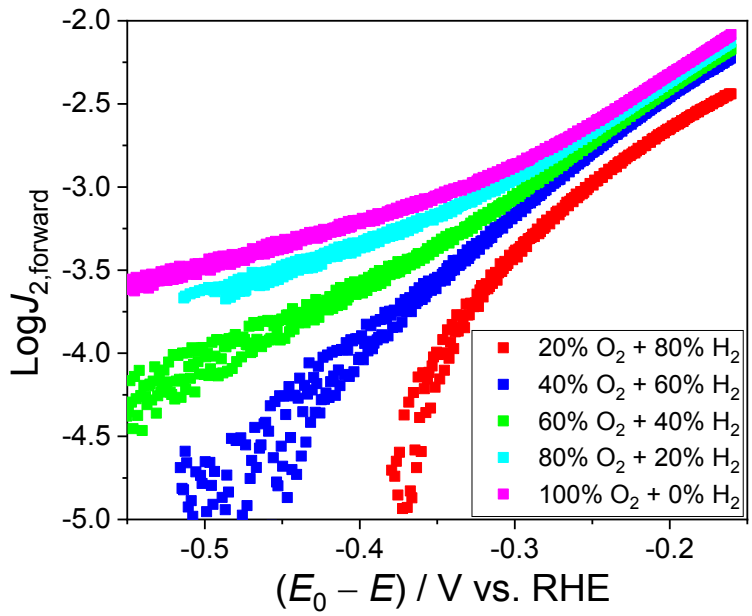

Figure S15. Log-linear plots of $J_{2,\mathrm{forward}}$ vs. ($E_0 - E$) for $SrTiO_3$/Pt electrodes with a (H_2 + O_2) gas mixture.

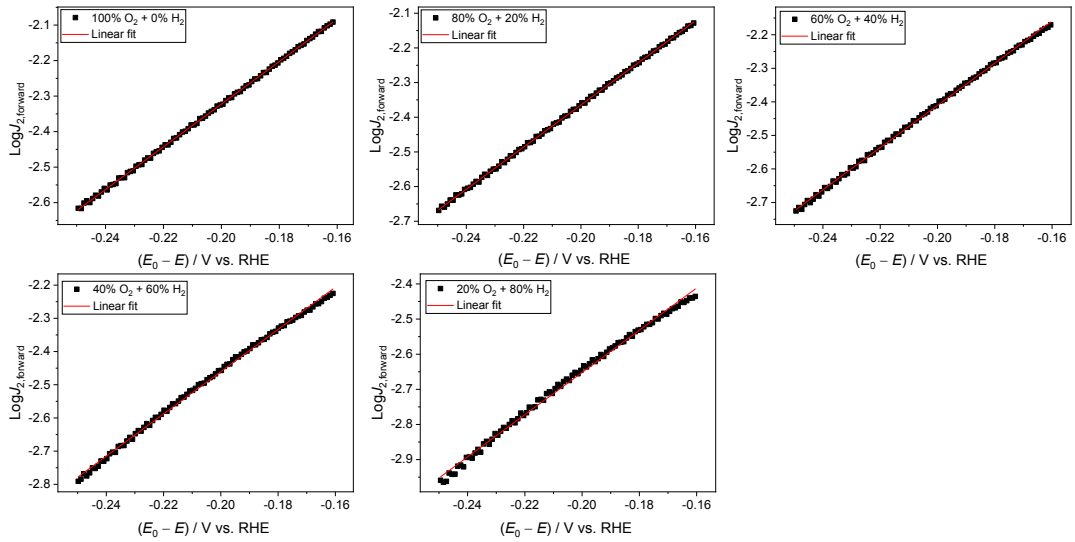

Figure S16. Linear fitting of log-linear plot of $J_{2,\mathrm{forward}}$ vs. $(E_0 - E)$ for $SrTiO_3$/Pt electrodes with a $(H_2 + O_2)$ gas mixture.

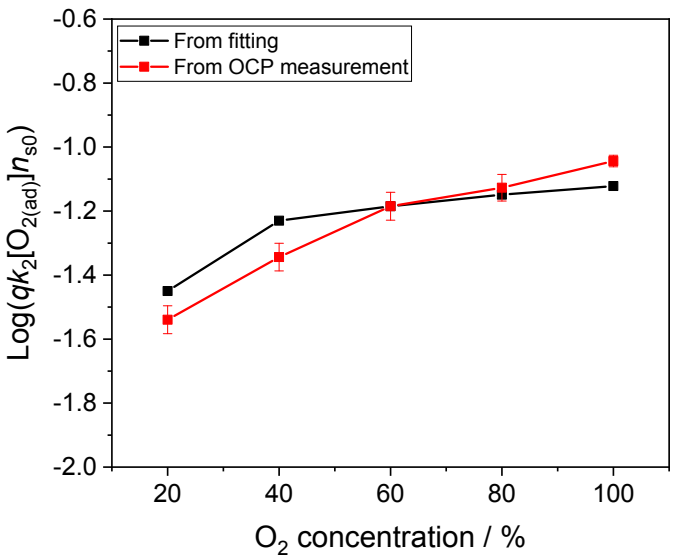

Figure S17. Values of $qk_2[O_{2(ad)}]n_{s0}$ from fitting and OCP measurement. For the convenience of comparison, the constant α was given a value which log(α) = − 2.6, where α is assigned as an arbitrary constant to present the relative ratios in Table S5. Error bars in the "OCP measurement" arose from the variation of OCPs measured in a 1-minute duration.

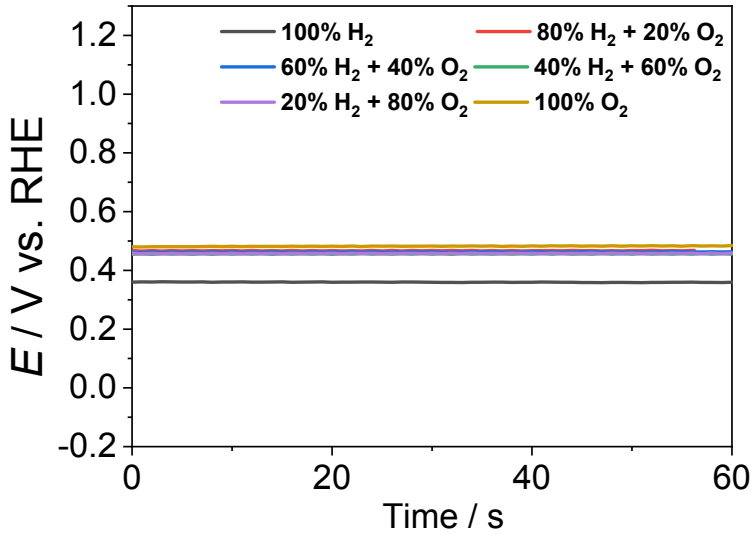

Figure S18. OCPs of a Ti layer by sputtering in an aqueous electrolyte purged with a (H_2 + O_2) gas mixture. The electrolyte is 0.5 M Na_2SO_4(aq) solution with pH adjusted to 12.5.

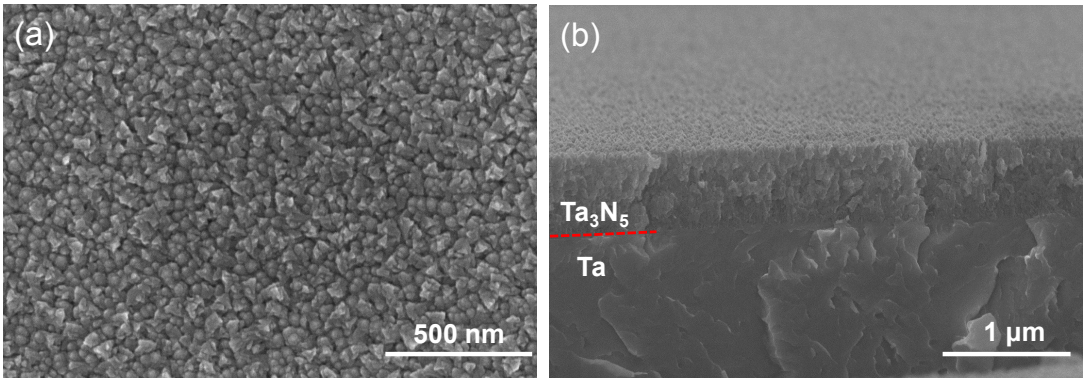

Figure S19. (a) Plan-view and (b) cross-sectional SEM images of a Ta_3N_5 film on a Ta substrate.

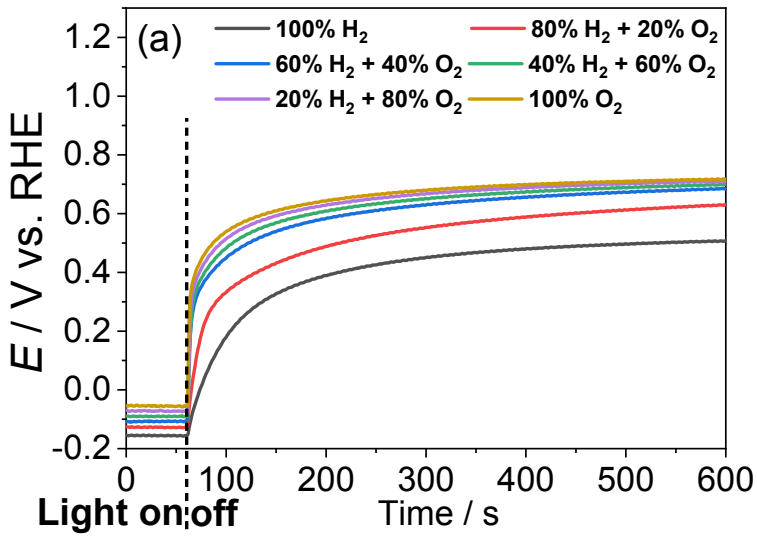
(a)
100% H2
80% H2 + 20% O2
60% H2 + 40% O2
40% H2 + 60% O2
20% H2 + 80% O2
100% O2
E / V vs. RHE
1.2
1.0
0.8
0.6
0.4
0.2
0.0
-0.2
0
100
200
300
400
500
600
Light on off
Time / s

813

814

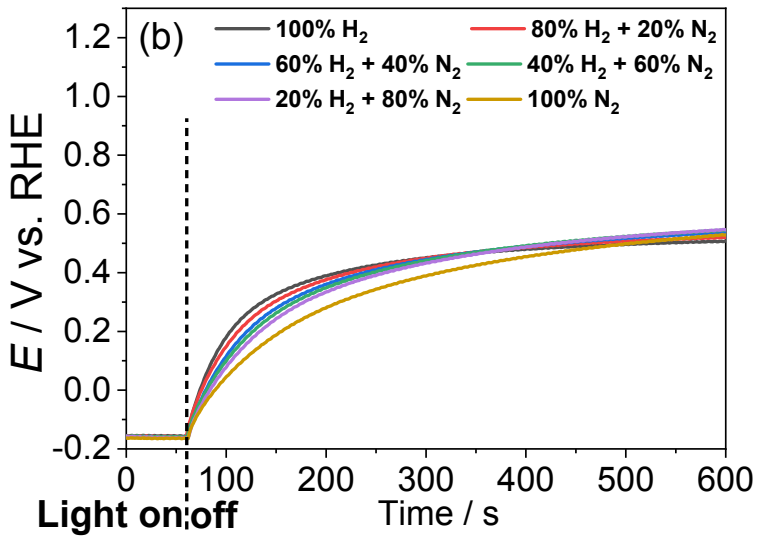
(b)
100% H2
80% H2 + 20% N2
60% H2 + 40% N2
40% H2 + 60% N2
20% H2 + 80% N2
100% N2
E / V vs. RHE
1.2
1.0
0.8
0.6
0.4
0.2
0.0
-0.2
0
100
200
300
400
500
600
Light on off
Time / s

815

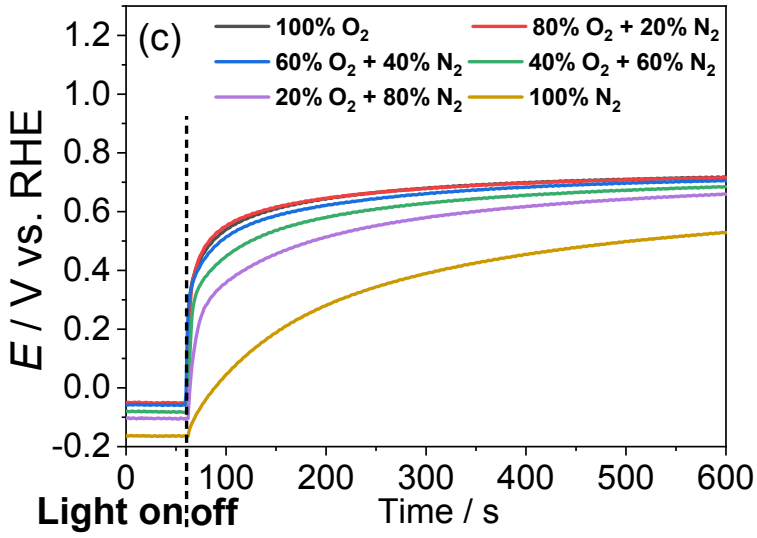

Figure S20. OCPs of a Ti/$SrTiO_3$:Al photoelectrode in an aqueous electrolyte purged with (a) a (H_2 + O_2) gas mixture, (b) a (H_2 + N_2) gas mixture, or (c) a (O_2 + N_2) gas mixture. The electrolyte is 0.5 M Na_2SO_4(aq) solution with pH adjusted to 12.5.

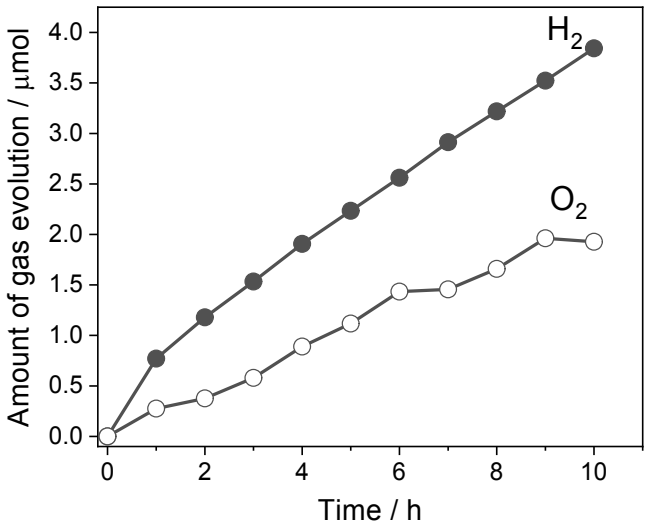

Figure S21. A time course of gas evolution during overall water splitting over $SrTiO_3$:Al particles. The reaction was conducted in de-ionized water.

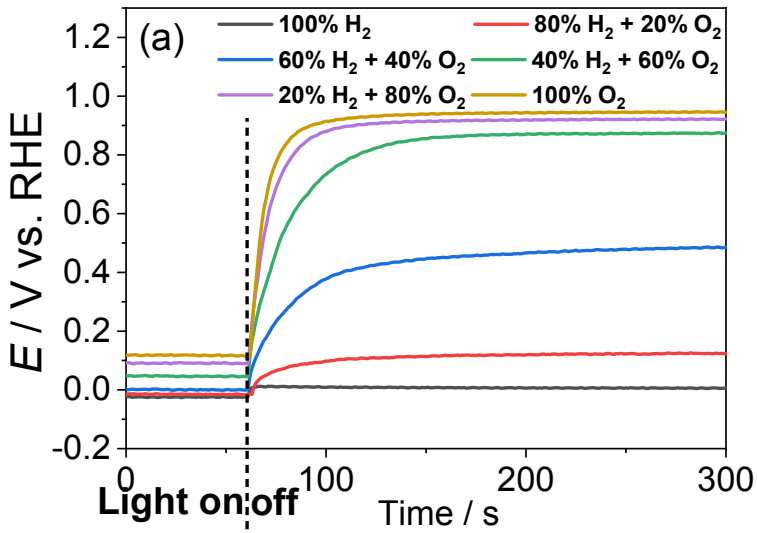
(a)
100% H2
80% H2 + 20% O2
60% H2 + 40% O2
40% H2 + 60% O2
20% H2 + 80% O2
100% O2
E / V vs. RHE
Time / s
Light on/off

825

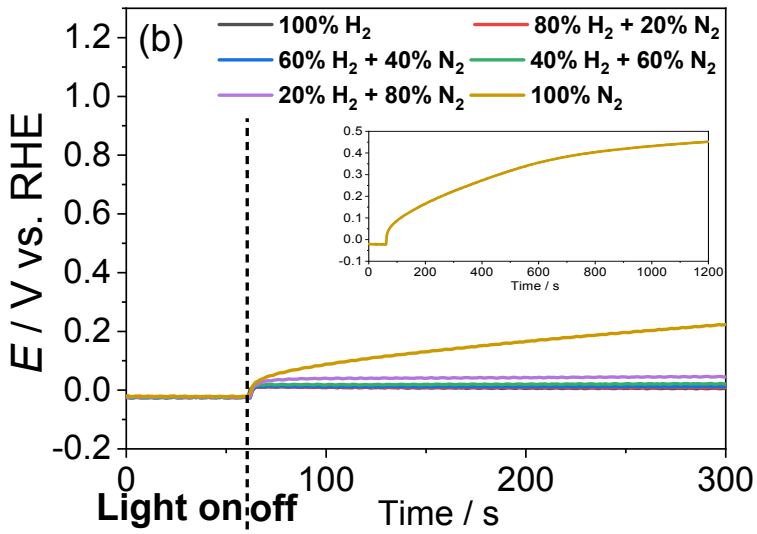
(b)
100% H2
80% H2 + 20% N2
60% H2 + 40% N2
40% H2 + 60% N2
20% H2 + 80% N2
100% N2
E / V vs. RHE
Time / s
Light on/off

826

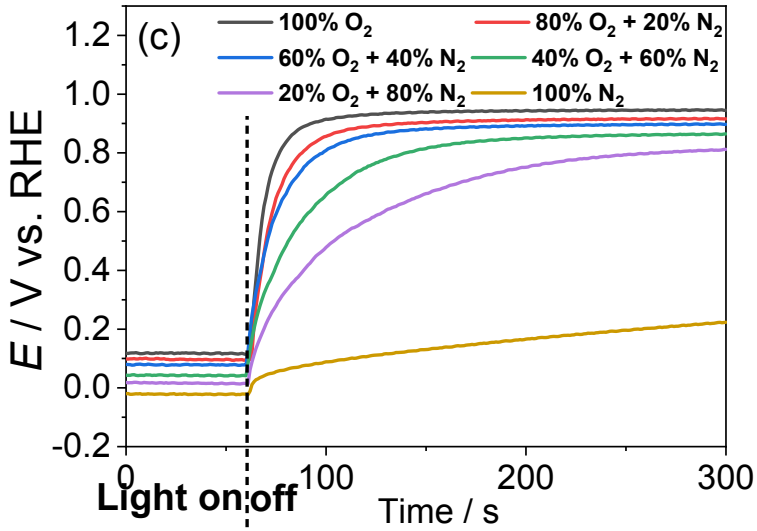

Figure S22. OCPs of a Ti/$SrTiO_3$:Al/Pt photoelectrode in an aqueous electrolyte purged with (a) a (H_2 + O_2) gas mixture, (b) a (H_2 + N_2) gas mixture, or (c) a (O_2 + N_2) gas mixture. Inset in (b): OCPs in an aqueous electrolyte purged with pure N_2 for 1200 s. The electrolyte is 0.5 M Na_2SO_4(aq) solution with pH adjusted to 12.5.

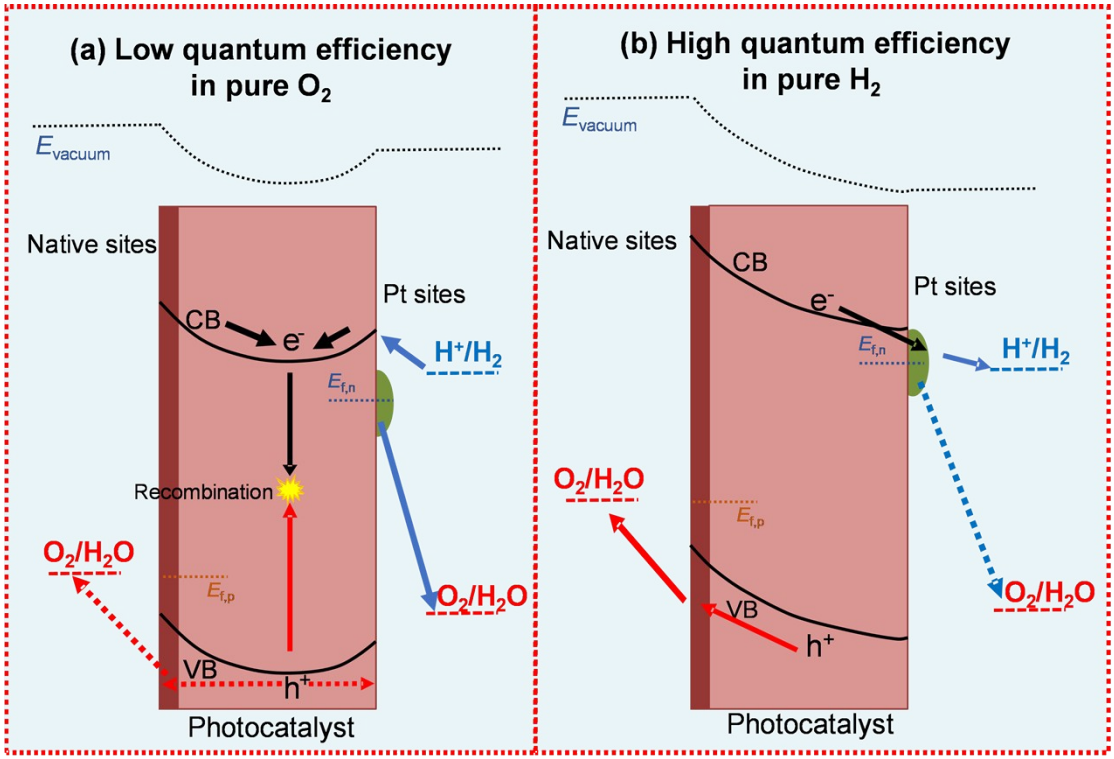

Figure S23. Energy diagrams of photocatalyst/co-catalyst/water junction in the dark with the electrolyte purged by (a) O_2 and (b) H_2. These energy diagrams are applicable to $SrTiO_3$/Pt/water, $SrTiO_3$:Al/Pt/water and Ta_3N_5/Pt/water liquid junction interfaces.

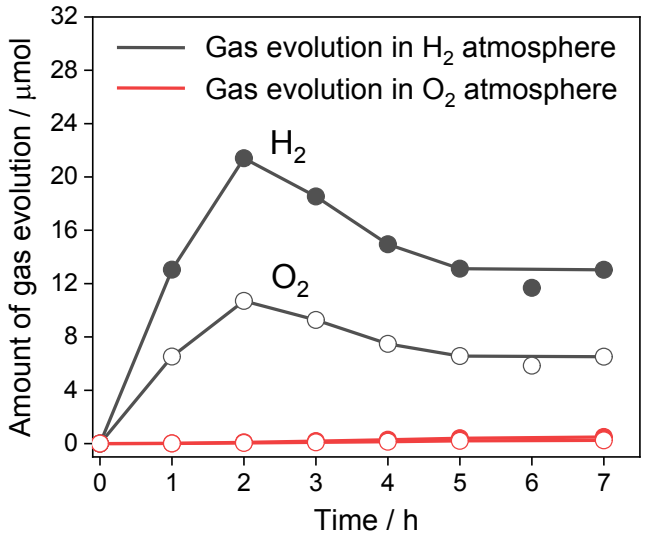

Figure S24. Time courses of gas evolution during overall water splitting over $SrTiO_3$:Al/Pt particles in H_2 and O_2 atmosphere. In H_2 atmosphere, (60% H_2 + 40% Ar) was used instead of 100% H_2 for safety concern. The produced H_2 cannot be accurately measured due to the high H_2 background concentration in (60% H_2 + 40% Ar) atmosphere. The amount of O_2 was measured. The amount of H_2 was calculated based on the water splitting stoichiometry. The water splitting occurred, but stopped after two hours due to the local accumulation of O_2 on particles. In O_2 atmosphere, 100% O_2 was used. The produced O_2 cannot be accurately measured due to the high O_2 background concentration in pure O_2 atmosphere. The amount of H_2 was measured to be negligible. The amount of O_2 was calculated to be negligible based on the water splitting stoichiometry. The reaction was conducted in de-ionized water.

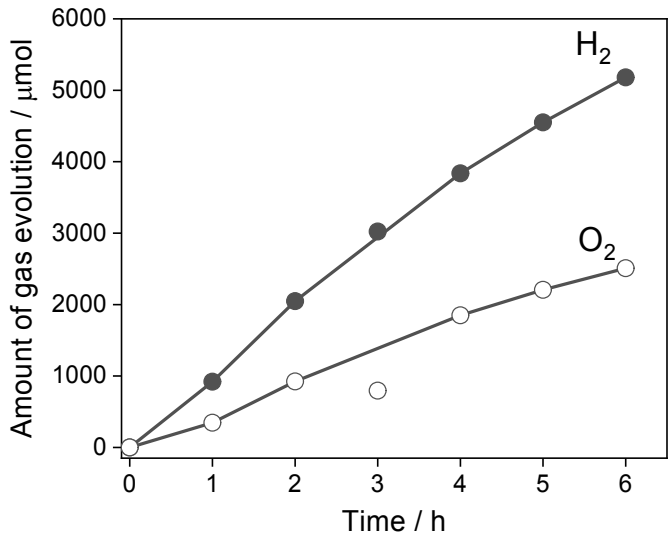

Figure S25. A time course of gas evolution during overall water splitting over $SrTiO_3$:Al/$RhCrO_x$ particles. The reaction was conducted in de-ionized water.

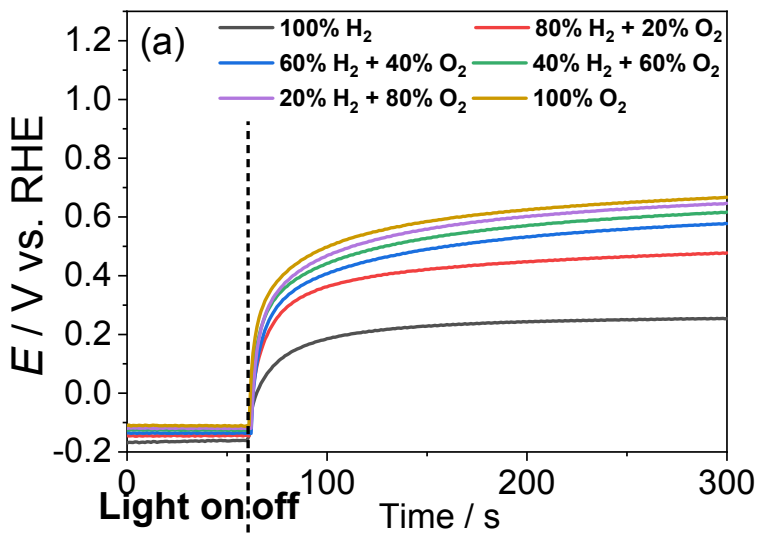

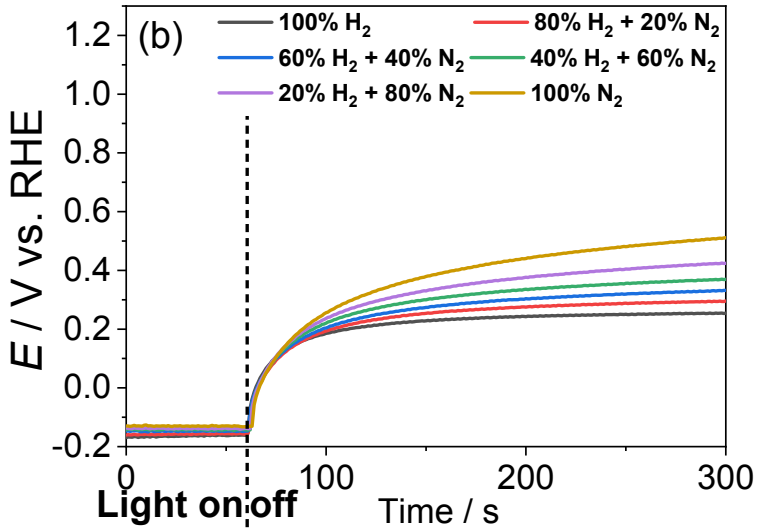

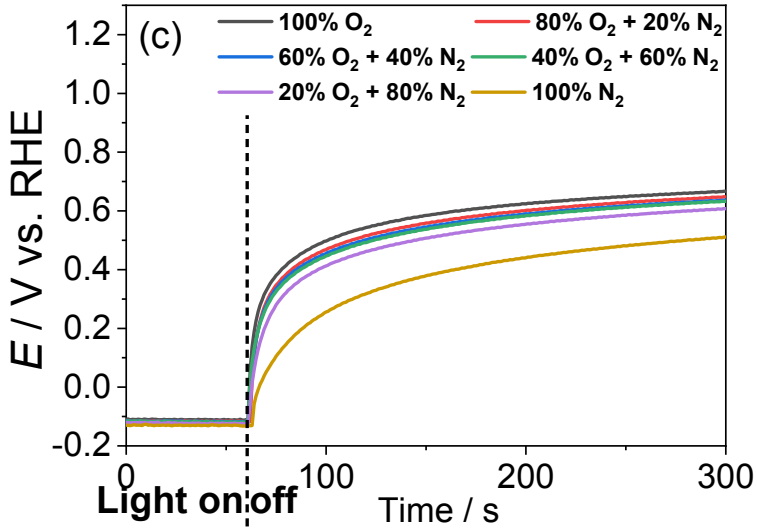

Figure S26. OCPs of a Ti/$SrTiO_3$:Al/$RhCrO_x$ photoelectrode in an aqueous electrolyte purged with (a) a (H_2 + O_2) gas mixture, (b) a (H_2 + N_2) gas mixture, or (c) a (O_2 + N_2) gas mixture. The electrolyte is 0.5 M Na_2SO_4(aq) solution with pH adjusted to 12.5.

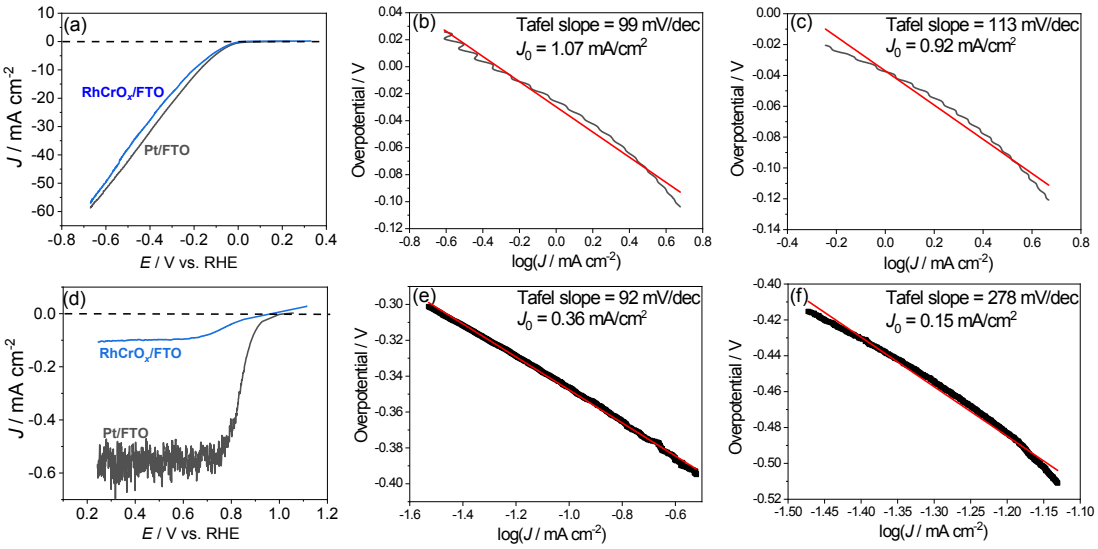

Figure S27. *J-E* curves for FTO/Pt and FTO/RhCrO$_x$ for (a) H_2 evolution in the electrolyte purged with H_2, and (d) O_2 reduction in the electrolyte purged with O_2. Tafel plots for (b) and (c) the H_2 evolution performance of Pt and RhCrO$_x$, and (e) and (f) the O_2 reduction performance of Pt and RhCrO$_x$. Black line: raw results; red line: Tafel fitting. The Tafel slope was calculated based on the iR-corrected polarization curves. The electrolyte is 0.5 M Na_2SO_4(aq) solution with pH adjusted to 12.5.

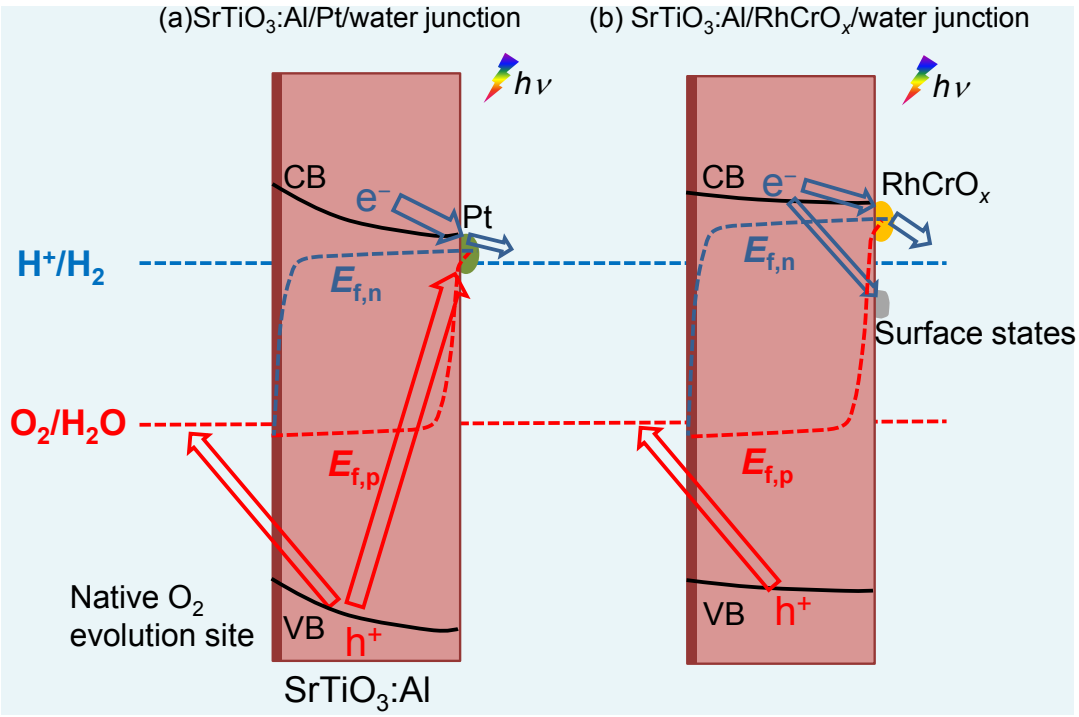

Figure S28. Schematic energy diagrams of (a) SrTiO$_3$:Al/Pt/water junction and (b) SrTiO$_3$:Al/RhCrO$_x$/water junction under illumination. The shaded region at at bare SrTiO$_3$ surfaces indicate the hole charge trapping sites that drive water oxidation.

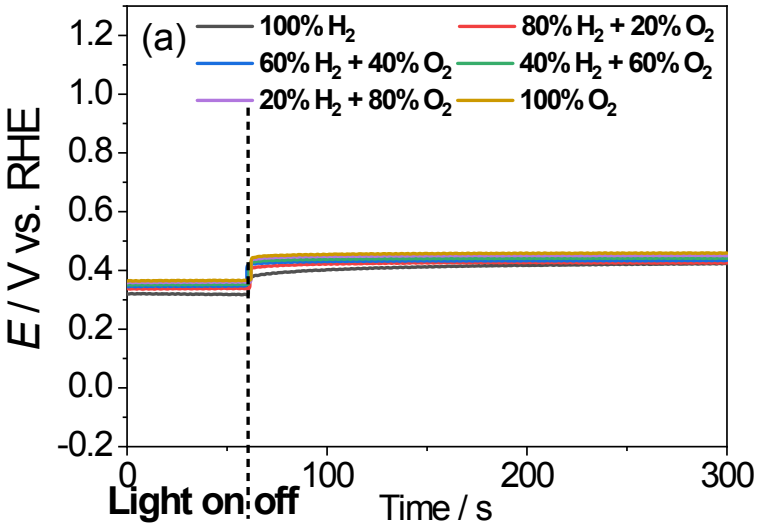
(a)
100% H2
80% H2 + 20% O2
60% H2 + 40% O2
40% H2 + 60% O2
20% H2 + 80% O2
100% O2
E / V vs. RHE
1.2
1.0
0.8
0.6
0.4
0.2
0.0
-0.2
0
100
200
300
Light on off
Time / s

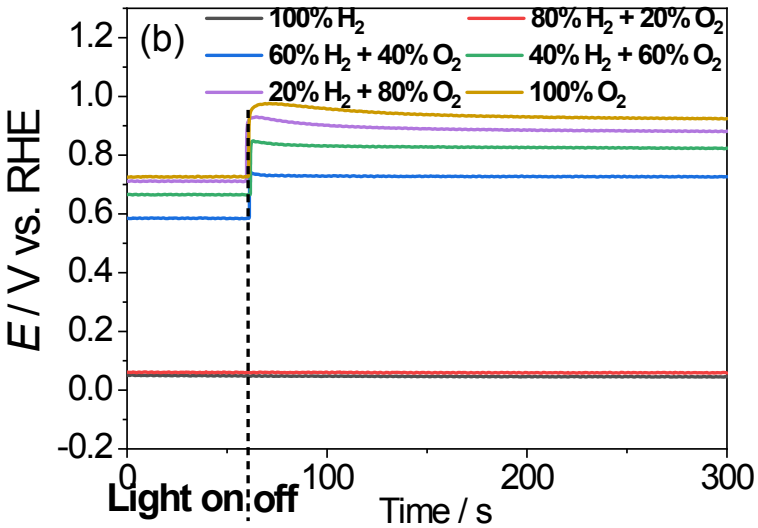
(b)
100% H2
80% H2 + 20% O2
60% H2 + 40% O2
40% H2 + 60% O2
20% H2 + 80% O2
100% O2
E / V vs. RHE
1.2
1.0
0.8
0.6
0.4
0.2
0.0
-0.2
0
100
200
300
Light on off
Time / s

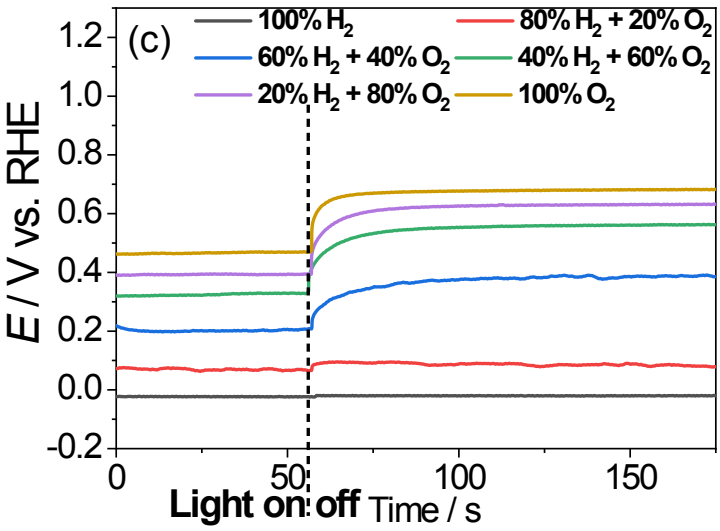

Figure S29. OCPs of (a) Ta/Ta_3N_5, and (b) $Ta/Ta_3N_5/Pt$ photoelectrodes in an aqueous electrolyte, and (c) $Ta/Ta_3N_5/Pt$ in 20 vol% MeOH aqueous solution purged with a (H_2 + O_2) gas mixture. The electrolyte is 0.5 M Na_2SO_4(aq) solution with pH adjusted to 12.5 for (a) and (b). The electrolyte is 0.5 M Na_2SO_4 20 vol% MeOH aqueous solution with pH adjusted to 12.5 for (c).

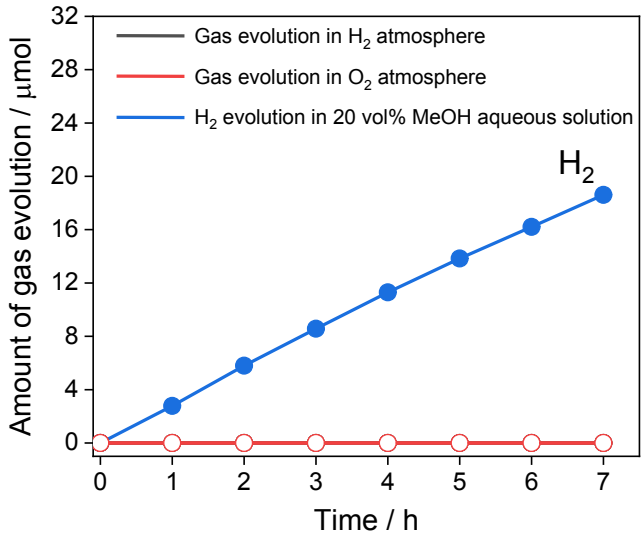

Figure S30. Time courses of gas evolution during overall water splitting and H_2 evolution during half reaction in 20 vol% MeOH aqueous solution over Ta_3N_5/Pt. In H_2 atmosphere, (60% H_2 + 40% Ar) was used instead of 100% H_2 for safety reasons. The amount of O_2 was measured, while the amount of H_2 was calculated by the water splitting stoichiometry. In O_2 atmosphere, 100% O_2 was used. The amount of H_2 was

measured, while the amount of O_2 was calculated by the water splitting stoichiometry. The data points of H_2 evolution and O_2 evolution during overall water splitting covered each other. N_2 evolution due to self-oxidation of Ta_3N_5 was not shown. Overall water splitting was conducted in de-ionized water. H_2 evolution during half reaction was conducted in 20 vol% MeOH aqueous solution.

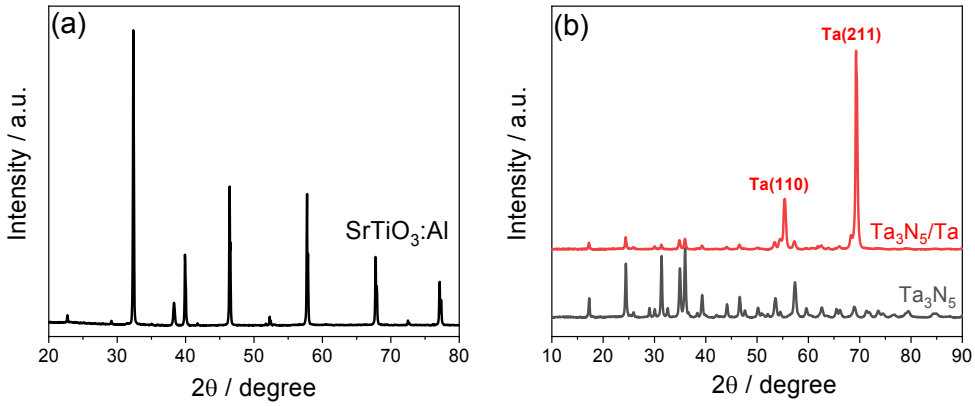

Figure S31. XRD patterns of (a) $SrTiO_3$:Al particles, and (b) Ta_3N_5/Ta and Ta_3N_5 particles.

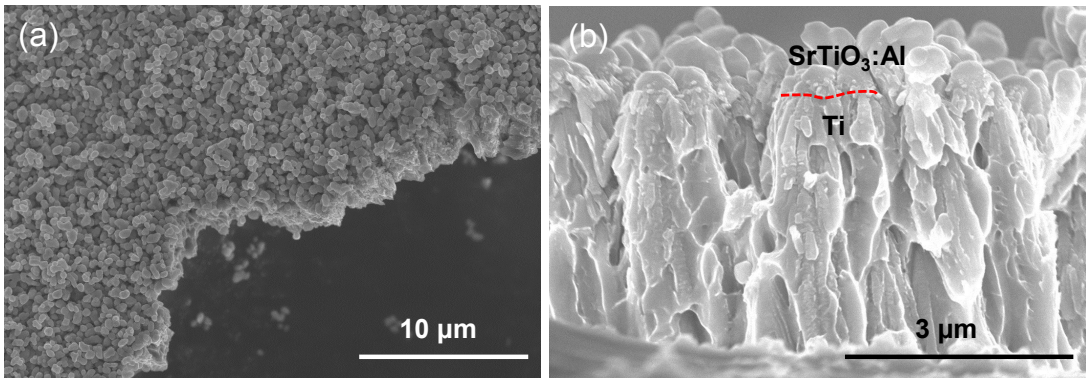

Figure S32. (a) Plan-view and (b) cross-sectional SEM images of $SrTiO_3$:Al particles on a Ti substrate.

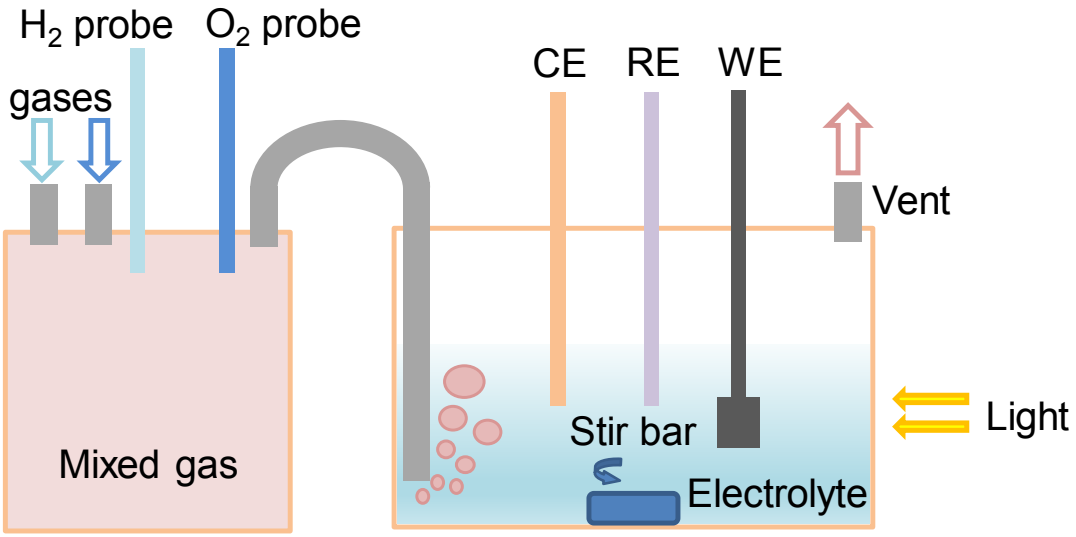

Figure S33. Schematic of electrochemical cell. H_2 (g), O_2 (g) and N_2 (g) were used for mixed gas. WE: working electrode; RE: reference electrode; CE: counter electrode. The reactor operated in ambient pressure.

Reference

1. M. S. Wrighton, A. B. Ellis, P. T. Wolczanski, D. L. Morse, H. B. Abrahamson and D. S. Ginley, *J. Am. Chem. Soc.* , 1976, 98, 2774-2779.
2. H. Uwe, R. Yoshizaki, T. Sakudo, A. Izumi and T. Uzumaki, *Japanese Journal of Applied Physics*, 1985, 24, 335.
3. Y. Ham, T. Hisatomi, Y. Goto, Y. Moriya, Y. Sakata, A. Yamakata, J. Kubota and K. Domen, *J. Mater. Chem. A*, 2016, 4, 3027-3033.
4. Z. Zhao, R. V. Goncalves, S. K. Barman, E. J. Willard, E. Byle, R. Perry, Z. Wu, M. N. Huda, A. J. Moulé and F. E. Osterloh, *Energy Environ. Sci.* , 2019, 12, 1385-1395.
5. T. Minegishi, N. Nishimura, J. Kubota and K. Domen, *Chem. Sci.*, 2013, 4, 1120-1124.
6. M. Zhong, T. Hisatomi, Y. Sasaki, S. Suzuki, K. Teshima, M. Nakabayashi, N. Shibata, H. Nishiyama, M. Katayama, T. Yamada and K. Domen, *Angew. Chem. Int. Ed.* , 2017, 56, 4739-4743.
7. E. Nurlaela, A. Ziani and K. Takanabe, *Materials for Renewable and Sustainable Energy*, 2016, 5, 18.
8. M. F. Lichterman, S. Hu, M. H. Richter, E. J. Crumlin, S. Axnanda, M. Favaro, W. Drisdell, Z. Hussain, T. Mayer, B. S. Brunschwig, N. S. Lewis, Z. Liu and H.-J. Lewerenz, *Energy Environ. Sci.* , 2015, 8, 2409-2416.
9. R. C. Rossi and N. S. Lewis, *J. Phys. Chem. B*, 2001, 105, 12303-12318.
10. S. M. S. K. K. Ng, *Wiley*, 2007.
11. Q. Wang, T. Hisatomi, Y. Suzuki, Z. Pan, J. Seo, M. Katayama, T. Minegishi, H. Nishiyama, T. Takata, K. Seki, A. Kudo, T. Yamada and K. Domen, *J. Am. Chem. Soc.* , 2017, 139, 1675-1683.
12. C. Song and J. Zhang, in *PEM Fuel Cell Electrocatalysts and Catalyst Layers: Fundamentals and Applications*, ed. J. Zhang, Springer London, London, 2008, DOI: 10.1007/978-1-84800-936-3_2, pp. 89-134.
13. A. Kumar, P. G. Santangelo and N. S. Lewis, *J. Phys. Chem.* , 1992, 96, 834-842.
14. Q. Wang, T. Hisatomi, Q. Jia, H. Tokudome, M. Zhong, C. Wang, Z. Pan, T. Takata, M. Nakabayashi, N. Shibata, Y. Li, I. D. Sharp, A. Kudo, T. Yamada and K. Domen, *Nat. Mater.* , 2016, 15, 611-615.
15. Q. Wang, T. Hisatomi, S. S. K. Ma, Y. Li and K. Domen, *Chem. Mater.* , 2014, 26, 4144-4150.
16. T. Wolfram and S. Ellialtioglu, *Electronic and optical properties of d-band perovskites*, Cambridge University Press, 2006.
17. T. Shinagawa, A. T. Garcia-Esparza and K. Takanabe, *Scientific Reports*, 2015, 5, 13801.
18. J. Qiu, H. Hajibabaei, M. R. Nellist, F. A. L. Laskowski, T. W. Hamann and S. W. Boettcher, *ACS Central Science*, 2017, 3, 1015-1025.
19. M. Yoshida, A. Yamakata, K. Takanabe, J. Kubota, M. Osawa and K. Domen, *J. Am. Chem. Soc.* , 2009, 131, 13218-13219.